International Journal of Multiphase Flow 66 (2014) 62–78

Contents lists available at ScienceDirect

International Journal of Multiphase Flow

journal homepage: www.elsevier.com/locate/ijmulflow

Towards the direct numerical simulation of nucleate boiling flows

S. Le Martelot [a,*], R. Saurel [a,b,c], B. Nkonga [d]

[a] RS2N, Bastidon de la Caou, 13360 Roquevaire, France
[b] University Institute of France, CNRS, IUSTI, 5 rue E. Fermi, 13453 Marseille Cedex 13, France
[c] Aix-Marseille University, CNRS, IUSTI, 5 rue E. Fermi, 13453 Marseille Cedex 13, France
[d] University of Nice, LJAD UMR CNRS 7351, Parc Valrose, 06108 Nice Cedex, France

ARTICLE INFO

Article history:
Received 19 September 2013
Received in revised form 27 June 2014
Accepted 29 June 2014
Available online 17 July 2014

Keywords:
Hyperbolic systems
Multifluid
Multiphase
Phase change
DNS
Preconditioning
HLLC

ABSTRACT

A flow model is built to capture evaporating interfaces separating liquid and vapour. Surface tension, heat conduction, Gibbs free energy relaxation and compressibility effects are considered. The corresponding flow model is hyperbolic, conservative and in agreement with the second law of thermodynamics. Phase transition is considered through Gibbs energy relaxation, in the same mind as in Saurel et al. (2008). Surface tension effects are modelled following the lines of Brackbill et al. (1992). There is thus no need to resolve the interface structure as jump conditions are inherent features of the model formulation. With the present approach, the same set of partial differential equations is solved everywhere, in pure fluids as well as in the captured diffuse interface. There is thus a unique hyperbolic flow solver that handles flow dynamics, interface motion and eventually acoustic wave dynamics. To make distinction between "pure" fluids and liquid–vapour mixture treatment, different sets of algebraic equations are considered in the relaxation solver. To guarantee accurate computation of the liquid and gas dynamics the preconditioned implicit scheme of LeMartelot et al. (2013) is adapted to the present boiling flow model. The model and method are validated against a one-dimensional test problem having exact solution. Multidimensional computations are then shown to illustrate method capabilities.

© 2014 Elsevier Ltd. All rights reserved.

Introduction

This paper deals with the numerical simulation of boiling flows with a DNS-like approach (Direct Numerical Simulation). This research topic has important applications in nuclear and space engineering, for example, and many other technical and environmental areas. Existing heat and mass exchange correlations (widely used in averaged multiphase flow models and codes) have important limitations. The error bar covers several orders of magnitude. Flow topology changes, from bubbly to separated flows with vapour film at walls, have dramatic consequences on heat exchanges. The main issue relies on the fact that averaged two-phase flow models are unable to account for flow topology changes. Therefore, DNS-like of boiling flows may help for the derivation of sub-scale models. However, this research area is difficult as liquid–gas interfaces are present, in conjunction with heat conduction, phase transition and surface tension effects. Only a few numerical approaches deal with such flows, the most natural being due to Tryggvason et al. (2001) and Juric and Tryggvason (1998), where the interface is considered as a sharp discontinuity, solved with a front tracking algorithm. The other approaches consider the interface as a diffuse zone.

With diffuse interface models, two different kinds of approaches have to be mentioned.

The first one takes essence in chemical–physics with the pioneer work of Cahn and Hilliard (1958), also called in the literature "second gradient theory" and "theory of Korteweg-type fluids". This theory works quite well in the vicinity of the thermodynamic critical point where liquid and vapour density become very close. The fluid density is considered as the order parameter and the fluid internal energy is considered as a function of the density and the density gradient. Considerable efforts have been done in this modelling direction (see Anderson et al. (1998) for example). Examples of computational works in this frame are reported in this last reference and in (Jamet et al., 2001). In addition to the very limited density ratio at interfaces, another limitation appears. Indeed, the interface capillary structure has to be resolved, which results in very fine meshes and associated computational limitations.

The second diffuse interface approach takes essence in discontinuity capturing methods and particularly Godunov contributions. In this frame, discontinuities are captured as a consequence of the conservative formulation of the equations. There is no need

* Corresponding author.
E-mail addresses: sebastien.lemartelot@gmail.com (S. Le Martelot), richard.saurel@univ-amu.fr (R. Saurel), boniface.nkonga@unice.fr (B. Nkonga).

http://dx.doi.org/10.1016/j.ijmultiphaseflow.2014.06.010
0301-9322/© 2014 Elsevier Ltd. All rights reserved.

to resolve the internal structure of discontinuities as jump conditions are present in the formulation. This approach has been competing with front tracking methods during the 70s, with artificial viscosity methods during the 80s, and is now used in nearly all computational codes dealing with gas dynamics equations and more generally with hyperbolic systems of conservation laws. The present work belongs to this class of approaches.

The diffuse interface approach based on multiphase descriptions of mixture cells with the help of hyperbolic systems with relaxation is due to (Saurel and Abgrall, 1999). This approach has shown its efficiency for the computation of flows in severe conditions, with arbitrarily high pressure and density ratios, with applications ranging from detonation physics (Petitpas et al., 2009; Saad, 1992; Saurel and Abgrall, 1999; Saurel et al., 2007; Saurel et al., 2008; Saurel et al., 2009; Schoch et al., 2013), shock waves in heterogeneous media, cavitating flows (Petitpas et al., 2009) to solid mechanics (Favrie et al., 2009). The difficulties are related to the models and numerical schemes building, especially when non-conservative equations are present. In this paper, low speed boiling flows are considered through a specific diffuse interfaces formulation.

To deal with interface zones in local mechanical and thermal equilibrium, a reduction of the Kapila et al. (2001) model is done. The model considered in the present paper is a temperature equilibrium version of the model derived in (Saurel et al., 2008). Mechanical and thermal equilibrium reduction is justified as, to model phase change, conductive heat transfer is needed. As a consequence there is no temperature discontinuity (in the frame of DNS like approach) at the interface and a single temperature model is appropriate. To be more precise, Kapila et al. (2001) model involves two temperatures and is well suited for interfaces computations as temperature and entropy discontinuities are present when the interface separates two non-miscible fluids, such as for example liquid water and air. When heat conduction is present, the temperature becomes continuous and a single temperature model is more appropriate. Indeed, the conduction layer has to be solved in the present context of boiling flows, as in flame computations. The temperature equilibrium model involves four partial differential equations only, is hyperbolic and conservative. Gibbs free energy relaxation terms are considered to model phase change. The flow model is in agreement with the second law of thermodynamics. It is reminiscent of the reactive Euler equations, widely used in combustion modelling. The main difference appears in the fact that each phase occupies its own volume, contrarily to gas mixtures, where each gas component occupies the entire volume. This difference has serious consequences regarding the thermodynamic closure. For gas mixtures, the mixture equation of state derives from the Dalton law. Here, it is derived from the mixture energy definition and temperature and pressure equilibrium conditions.

From the basic temperature equilibrium flow model with four partial differential equations, extra physics is added to deal with boiling flows. Surface tension effects are modelled with Brackbill et al. (1992) method, already considered in the context of compressible fluids (Perigaud and Saurel, 2005). Heat conduction and gravity effects are also added.

The second issue addressed in the paper is related to the numerical approximation of the flow model, especially hyperbolic and elliptic parts, capillary terms and thermochemical relaxation.

The hyperbolic step is solved with a variant of the preconditioned implicit hyperbolic solver detailed in (LeMartelot et al., 2013). It is an extension of Guillard and Viozat (1999) method for low Mach number flows, this method being itself a conservative and time accurate extension of Turkel (1987) preconditioning algorithm.

The relaxation solver used to fulfil interface conditions of evaporating interfaces is detailed with particular attention paid to the single phase limit. The hyperbolic and relaxation solvers are then combined to solve the flow model in 1D, obviously in absence of capillary effects, to check model and method convergence against an exact solution of sharp evaporating interface. Convergence being reached in 1D, computational boiling flows examples are shown in 2D with the various needed physical effects. A 2D configuration with several bubbles is considered and computed. From this first computation, a new physical feature appears, never reported before in the authors knowledge. Starting from an initial situation where some nucleation sites are present, bubbles appear dynamically from the sites location, but also from other locations where perfect wall conditions are used. The bubbles appearance and size selection thus appear as a self sustained process independent of nucleation sites. Dynamic interfaces appearance was a feature already observed in the context of cavitating flows, using the temperature non-equilibrium model shown in section 'Out of equilibrium model'.

Model building

The starting point of the analysis relies on the mechanical equilibrium, temperatures non-equilibrium flow model of Kapila et al. (2001), where heat and mass exchanges have been inserted (Saurel et al., 2008).

Out of equilibrium model

The model given in the last reference reads:

$$\frac{\partial \alpha_1}{\partial t} + \mathbf{u} \bullet \mathbf{grad}(\alpha_1) = \frac{\rho_2 c_2^2 - \rho_1 c_1^2}{\frac{\rho_1 c_1^2}{\alpha_1} + \frac{\rho_2 c_2^2}{\alpha_2}} \mathrm{div}(\mathbf{u}) + \rho v (g_2 - g_1) \frac{\frac{c_1^2}{\alpha_1} + \frac{c_2^2}{\alpha_2}}{\frac{\rho_1 c_1^2}{\alpha_1} + \frac{\rho_2 c_2^2}{\alpha_2}} + \frac{\frac{\Gamma_1}{\alpha_1} + \frac{\Gamma_2}{\alpha_2}}{\frac{\rho_1 c_1^2}{\alpha_1} + \frac{\rho_2 c_2^2}{\alpha_2}} H(T_2 - T_1),$$

$$\begin{aligned}
&\frac{\partial \alpha_1 \rho_1}{\partial t} + \mathrm{div}(\alpha_1 \rho_1 \mathbf{u}) = \rho v (g_2 - g_1), \\
&\frac{\partial \alpha_2 \rho_2}{\partial t} + \mathrm{div}(\alpha_2 \rho_2 \mathbf{u}) = -\rho v (g_2 - g_1), \\
&\frac{\partial \rho \mathbf{u}}{\partial t} + \mathrm{div}\left(\rho \mathbf{u} \otimes \mathbf{u} + P \underline{I}\right) = 0, \\
&\frac{\partial \rho E}{\partial t} + \mathrm{div}((\rho E + P)\mathbf{u}) = 0.
\end{aligned} \tag{1}$$

The total energy is defined as $E = Y_1 e_1 + Y_2 e_2 + \frac{1}{2}\mathbf{u} \bullet \mathbf{u}$ where $Y_k = \frac{\alpha_k \rho_k}{\rho}$ represent the mass fractions and $\rho = \sum_k (\alpha_k \rho_k)$ the mixture density. This model is hyperbolic with the same wave speeds as the gas dynamics equations but with Wood (1930) sound speed, c_w, which presents a non monotonic behaviour with respect to the volume fractions (α_k),

$$\frac{1}{\rho c_w^2} = \sum_k \frac{\alpha_k}{\rho_k c_k^2}, \tag{2}$$

where c_k represents the sound speed associated to phase k.

It is worth to mention that the sound speed is always defined, provided that each phase has a convex equation of state. This feature is not satisfied by mixture flow based on cubic equations of state, like the Van der Waals one. The present equation of state providing the thermodynamic closure is obtained from the mixture energy definition and the pressure equilibrium condition. This equation of states involves at least three argument: $P = P(\rho, e, \alpha_1)$. For example, when each phase obeys the stiffened gas equation of state (see Le Métayer et al. (2004) for parameters determination),

$$p_k = (\gamma_k - 1)\rho_k (e_k - q_k) - \gamma_k P_{\infty,k}, \tag{3}$$

the mixture equation of state then reads,

$$P(\rho,e,\alpha_1)=\frac{\rho e-(\frac{\alpha_1\gamma_1P_{\infty,1}}{\gamma_1-1}+\frac{\alpha_2\gamma_2P_{\infty,2}}{\gamma_2-1})-\alpha_1\rho_1q_1-\alpha_2\rho_2q_2}{\frac{\alpha_1}{\gamma_1-1}+\frac{\alpha_2}{\gamma_2-1}}. \tag{4}$$

Parameters q_k,γ_k and $P_{\infty,k}$ are constants and depend on the material k. When dealing with phase transition applications, their determination is based on the saturation curves of the phase diagram. As this model involves a single pressure but two mass equations and a volume fraction equation, it is possible to determine two temperatures $(T_k=T_k(p,\rho_k))$ and two entropies.

This last feature is useful for phase transition modelling. System (1) is complemented by the mixture entropy equation,

$$\frac{\partial\rho S}{\partial t}+\mathrm{div}(\rho S\mathbf{u})=\frac{H(T_2-T_1)^2}{\rho}+\frac{\rho v(g_2-g_1)^2}{T_I}, \tag{5}$$

where T_I represents the "interface temperature" defined as $T_I=\frac{\frac{\Gamma_1T_1}{\alpha_1}+\frac{\Gamma_2T_2}{\alpha_2}}{\frac{\Gamma_1}{\alpha_1}+\frac{\Gamma_2}{\alpha_2}}$, showing agreement with the second law of thermodynamics.

Some comments are due regarding the volume fraction equation. The first term in the right hand side, present in Kapila et al. (2001) model, represents mechanical relaxation effects, present in all zones where the velocity divergence is non-zero (shocks, compressions, expansions). The second term represents volume variations due to mass transfer, in a context where both phases are compressible. The last group of terms represents dilatation effects due to heat transfer. Γ_k represents the Grüneisen coefficient of phase k.

System (1) being non-conservative, non conventional shock relations have to be determined. Appropriate set of jump conditions is given in (Saurel et al., 2007). Heat and mass transfer in System (1) are considered as kinetic processes, controlled respectively by relaxation rates H and v. The Gibbs free energies are denoted by $g_k=h_k-T_ks_k$.

The degrees of freedom with this model are related to the relaxation rates H and v. When the fluids in contact at an interface are non-miscible (liquid water and air for example) H and v are set to zero, allowing the jump conditions of equal normal velocities and pressures to be satisfied. Computational examples and comparisons with exact solutions are given in (Saurel et al., 2009). When phase transition occurs at the interface between a liquid and its vapour, provided that one of the phase is metastable (overheated or subcooled), local thermodynamic equilibrium is assumed, meaning that phase transition occurs infinitely fast (infinite H and v). As relaxation parameters are set to infinite only locally, phase transition fronts propagating at global finite rate (Saurel et al., 2008) are correctly reproduced, at least for flashing flow situations. To remove the difficulty related to the resolution of stiff differential systems, relaxation solvers have been built in the same reference and in (LeMartelot et al., 2013).

This model is thus able to deal with simple contact interface and evaporating (or condensing) interfaces when heat and mass relaxation coefficients are considered and stiff. To illustrate model's capabilities, Fig. 1 shows a computational example of cavitating underwater rocket involving these two kinds of interfaces.

The main goal being the simulation of boiling flows, it is mandatory to consider heat diffusion. Therefore, flow model (1) can be reduced to consider a single temperature.

Temperature equilibrium model

In the limit of stiff temperature relaxation (infinite H), System (1) reduces to:

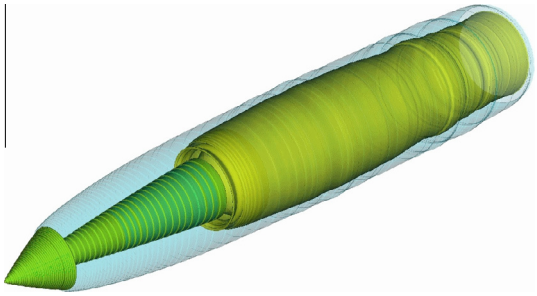

Fig. 1. Cavitating flow around a hypervelocity underwater rocket. Combustion gases issued from a rocket motor are located on the right hand side of the picture and are in contact with vapour. The vapour is separated from the liquid (not shown) by an evaporating interface. Two different types of interfaces are thus present in this example. Picture taken from Petitpas et al. (2009).

$$\begin{aligned}
&\frac{\partial\rho}{\partial t}+\mathrm{div}(\rho\mathbf{u})=0,\\
&\frac{\partial\rho\mathbf{u}}{\partial t}+\mathrm{div}\left(\rho\mathbf{u}\otimes\mathbf{u}+P\underline{\underline{I}}\right)=0,\\
&\frac{\partial\rho E}{\partial t}+\mathrm{div}((\rho E+P)\mathbf{u})=0,\\
&\frac{\partial\rho Y_1}{\partial t}+\mathrm{div}(\rho Y_1\mathbf{u})=\rho v(g_2-g_1).
\end{aligned} \tag{6}$$

This system is completed with the following entropy equation, where S denotes the mixture entropy:

$$\frac{\partial\rho S}{\partial t}+\mathrm{div}(\rho S\mathbf{u})=\frac{\rho v(g_2-g_1)^2}{T}. \tag{7}$$

The total energy is still defined by $E=Y_1e_1+Y_2e_2+\frac{1}{2}\mathbf{u}\bullet\mathbf{u}$. Formally, System (6) is reminiscent of the reactive Euler equations, widely used in combustion modelling. However, a fundamental difference appears regarding the thermodynamic closure. In combustion modelling, mixtures of gases are considered and the Dalton law is used to compute the pressure. Dalton law states that each constituent occupies the entire volume. This is not the case with two-phase mixtures where the fluids are separated by interfaces, each one of them occupying its own volume. To determine the thermodynamic closure of System (6), let's first consider the mixture specific volume definition,

$$v=Y_1v_1+Y_2v_2. \tag{8}$$

With the help of the caloric equation of state for a given phase,

$$e_k=C_{v,k}T+\frac{P_{\infty,k}}{\rho_k}+q_k, \tag{9}$$

the SG EOS (3) becomes,

$$p_k=(\gamma_k-1)\rho_kC_{v,k}T-P_{\infty,k}, \tag{10}$$

and the specific volume for a given phase can be expressed as:

$$v_k=\frac{(\gamma_k-1)C_{v,k}T}{p+P_{\infty,k}} \tag{11}$$

A first relation resulting of (8) and (11) is thus obtained, linking temperature, pressure and mixture specific volume:

$$\frac{1}{T}=\frac{1}{T(P,v,Y_1)}=\frac{Y_1(\gamma_1-1)C_{v,1}}{v(P+P_{\infty,1})}+\frac{Y_2(\gamma_2-1)C_{v,2}}{v(P+P_{\infty,2})}. \tag{12}$$

We now consider the mixture energy definition,

$$e=Y_1e_1+Y_2e_2. \tag{13}$$

Combining (9) and (11), the specific internal energy for a given phase reads:

$$e_k = C_{v,k} T \frac{P + \gamma_k P_{\infty,k}}{P + P_{\infty,k}} + q_k. \tag{14}$$

The mixture energy definition (13) becomes:

$$\frac{1}{T} = \frac{1}{T(P, e, Y_1)} = \frac{Y_1 C_{v,1} + \frac{Y_1(\gamma_1 - 1)C_{v,1}P_{\infty,1}}{P+P_{\infty,1}} + Y_2 C_{v,2} + \frac{Y_2(\gamma_2 - 1)C_{v,2}P_{\infty,2}}{P+P_{\infty,2}}}{e - (Y_1 q_1 + Y_2 q_2)} \tag{15}$$

Combining relations (12) and (15), the following equation linking the pressure, the mixture specific volume, the mixture energy and the mass fractions is obtained:

$$\rho\left[\frac{Y_1(\gamma_1 - 1)C_{v,1}}{P + P_{\infty,1}} + \frac{Y_2(\gamma_2 - 1)C_{v,2}}{P + P_{\infty,2}}\right] - \frac{Y_1 C_{v,1} + \frac{Y_1(\gamma_1 - 1)C_{v,1}P_{\infty,1}}{P+P_{\infty,1}} + Y_2 C_{v,2} + \frac{Y_2(\gamma_2 - 1)C_{v,2}P_{\infty,2}}{P+P_{\infty,2}}}{e - (Y_1 q_1 + Y_2 q_2)} = 0 \tag{16}$$

It corresponds to a quadratic function of the pressure. When one of the phases is a gas ($P_{\infty,gas} = 0$), as in the present context, the positive root is given by:

$$P = P(\rho, e, Y_1) = \frac{1}{2}(A_1 + A_2 - (P_{\infty,1} + P_{\infty,2})) + \sqrt{\frac{1}{4}(A_2 - A_1 - (P_{\infty,2} - P_{\infty,1}))^2 + A_1 A_2} \tag{17}$$

where $A_k = \frac{Y_k(\gamma_k - 1)Cv_k}{Y_1 Cv_1 + Y_2 Cv_2}(\rho(e - q) - P_{\infty,k})$ and $q = Y_1 q_1 + Y_2 q_2$.

Hyperbolicity and sound speed

System (6) is hyperbolic with three wave speeds, $\lambda_0 = u$ (two times fold), $\lambda_1 = u + c$ and $\lambda_2 = u - c$ with the following square sound speed:

$$c^2 = \frac{1}{2}\left((e - q)(a_1 + a_2) + \frac{\frac{1}{2}\left(\frac{\partial R_1}{\partial \rho}\right)_e R_1 + \left(\frac{\partial R_2}{\partial \rho}\right)_e}{\sqrt{\frac{1}{4}R_1 R_1 + R_2}} + \frac{P}{\rho^2}\left(\rho(a_1 + a_2) + \frac{\frac{1}{2}\left(\frac{\partial R_1}{\partial e}\right)_\rho R_1 + \left(\frac{\partial R_2}{\partial e}\right)_\rho}{\sqrt{\frac{1}{4}R_1 R_1 + R_2}}\right)\right) \tag{18}$$

where

$$a_1 = \frac{Y_1(\gamma_1 - 1)Cv_1}{Y_1 Cv_1 + Y_2 Cv_2}, a_2 = \frac{Y_2(\gamma_2 - 1)Cv_2}{Y_1 Cv_1 + Y_2 Cv_2},$$
$$R_1 = a_2\rho(e - q) - a_2 P_{\infty,2} - a_1\rho(e - q) + a_1 P_{\infty,1} - P_{\infty,2} + P_{\infty,1},$$
$$R_2 = a_1 a_2(\rho(e - q) - P_{\infty,1})(\rho(e - q) - P_{\infty,2}).$$

This sound speed can be compared to the Wood's sound speed (2). As Wood's sound speed deals with multiphase mixtures in mechanical equilibrium but out of thermal equilibrium, it should be always greater than the sound speed given by (18). This behaviour is illustrated in Fig. 2.

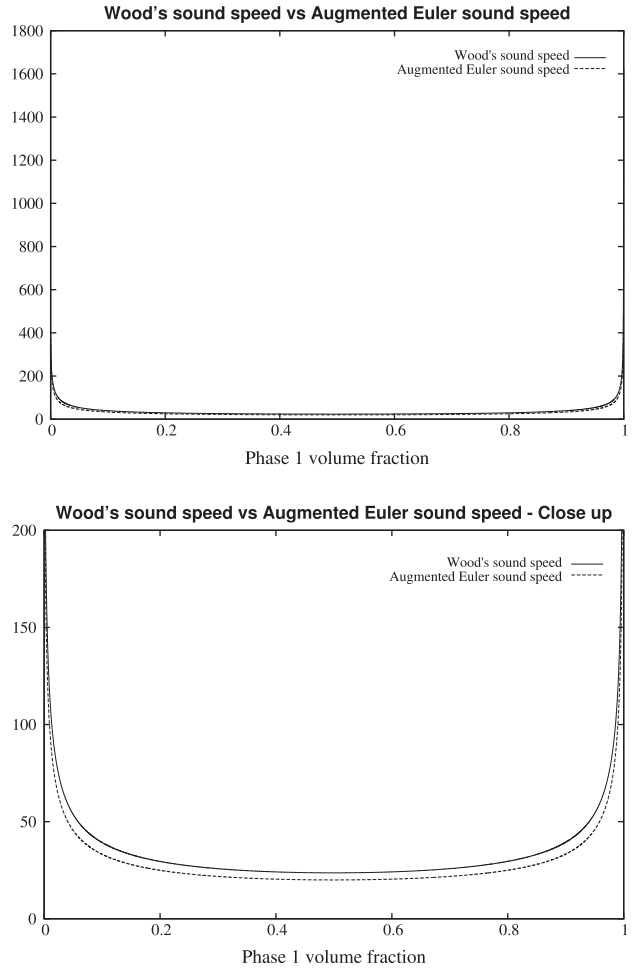

Fig. 2. The sound speed of System (6) given by (18) is compared to the Wood sound speed (2). Full view and close up.

Extra physics modelling

To deal with DNS of boiling flows, System (6) has to be complemented with extra physical effects, such as:

- buoyancy,
- surface tension,
- heat conduction,
- phase transition.

This list can be completed by extra effects, as for example, viscous ones, but we prefer to focus on those which are absolutely necessary. Modelling of the various effects is addressed gradually hereafter.

Surface tension effects are considered through the Continuum Surface Force (CSF) method of Brackbill et al. (1992). The capillary force is modelled as,

$$\mathbf{F}_\sigma = \sigma\kappa\overrightarrow{\nabla C}, \tag{19}$$

where σ represents the surface tension coefficient (N m^{-1}), κ represents the local curvature (m^{-1}) and C is a colour function used to locate the interface between the two phases and to compute the local curvature,

$$\kappa = -\mathrm{div}\left(\frac{\overrightarrow{\nabla C}}{|\overrightarrow{\nabla C}|}\right). \tag{20}$$

In this paper, the chosen colour function is the mass fraction of phase 1, Y_1, as this variable is invariant across shock and expansion waves. It varies at interfaces only.

The gravity force is modelled as:

$$\mathbf{F}_g = \rho\mathbf{g},$$

where $\mathbf{g}$ represents the gravity field.

Heat conduction is inserted in the total energy equation of the model through the Fourier law $\mathbf{q} = -\lambda_c\overrightarrow{\nabla T}$ where the "mixture" thermal conductivity is given by $\lambda_c = \alpha_1\lambda_1 + \alpha_2\lambda_2$ and λ_k represents the thermal conductivity of phase k. The asymptotic analysis leading to this formulation is summarised Appendix A.

Phase transition is addressed following (Saurel et al., 2008) through Gibbs free energy relaxation. Stiff relaxation is considered to fulfil the chemical potential equality at the interface: $(g_1)_I = (g_2)_I$. This relaxation process is used at each mesh point with some subtleties regarding "pure" fluid cells and cases of total evaporation or total condensation. Details are given in Appendix B.

Adding the extra effects mentioned previously, the following general model is obtained:

$$\begin{aligned}
&\frac{\partial \rho Y_1}{\partial t} + \operatorname{div}(\rho Y_1 \mathbf{u}) = \rho v (g_2 - g_1),\\
&\frac{\partial \rho}{\partial t} + \operatorname{div}(\rho \mathbf{u}) = 0,\\
&\frac{\partial \rho \mathbf{u}}{\partial t} + \operatorname{div}\left(\rho \mathbf{u} \otimes \mathbf{u} + P\underline{\underline{I}}\right) = \sigma\kappa\overrightarrow{\nabla Y_1} + \rho\mathbf{g},\\
&\frac{\partial \rho E}{\partial t} + \operatorname{div}((\rho E + P)\mathbf{u}) = \operatorname{div}\left(\lambda_c \overrightarrow{\nabla T}\right) + \sigma\kappa\overrightarrow{\nabla Y_1} \bullet \mathbf{u} + \rho\mathbf{g} \bullet \mathbf{u}.
\end{aligned} \tag{21}$$

A conservative form is available:

$$\begin{aligned}
&\frac{\partial \rho Y_1}{\partial t} + \operatorname{div}(\rho Y_1 \mathbf{u}) = \rho v (g_2 - g_1),\\
&\frac{\partial \rho}{\partial t} + \operatorname{div}(\rho \mathbf{u}) = 0,\\
&\frac{\partial \rho \mathbf{u}}{\partial t} + \operatorname{div}\left(\rho \mathbf{u} \otimes \mathbf{u} + P\underline{\underline{I}} - \sigma\left(|\mathbf{m}|\underline{\underline{I}} - \frac{\mathbf{m} \otimes \mathbf{m}}{|\mathbf{m}|}\right)\right) = \rho\mathbf{g},\\
&\frac{\partial \rho E + \sigma|\mathbf{m}|}{\partial t} + \operatorname{div}\Big((\rho E + P + \sigma|\mathbf{m}|)\mathbf{u}\\
&\quad -\sigma\left(|\mathbf{m}|\underline{\underline{I}} - \frac{\mathbf{m} \otimes \mathbf{m}}{|\mathbf{m}|}\right) \bullet \mathbf{u} - \lambda_c \overrightarrow{\nabla T}\Big) = \rho\mathbf{g} \bullet \mathbf{u}.
\end{aligned} \tag{22}$$

This system is closed by the EOS (17). Hyperbolicity is preserved through the waves speeds given in section 'Hyperbolicity and sound speed'. The entropy equation associated with System (21) reads,

$$\frac{\partial \rho S}{\partial t} + \operatorname{div}\left(\rho S\mathbf{u} - \frac{\lambda_c \overrightarrow{\nabla T}}{T}\right) = \frac{\rho v (g_2 - g_1)^2}{T} + \lambda_c \frac{(\nabla T)^2}{T^2}, \tag{23}$$

and shows agreement with the second law of thermodynamics.

System (22) is considered hereafter to compute boiling flow configurations.

Numerical method

Introduction

In this section we address the numerical methods used to approximate solutions of System (21). The numerical strategy is based on an operator splitting technique with a hyperbolic subsystem where capillary and gravity forces are removed. This leads to simplified Riemann solver, but with some unbalanced forces that can produce spurious effects. However, the use of an implicit scheme results, in the presence context, in negligible spurious effects that do not affect the global accuracy and stability. This is consistent with the analysis performed in (Braconnier and Nkonga, 2009) where capillary forces are included in the hyperbolic solver.

In addition, numerical simulation of boiling flows leads to two main types of numerical issues. The first one is related to the presence of compressible effects in conjunction with low Mach number conditions. As the flow speed is low ($\simeq$1 m/s) the use of compressible flow formulation lead to very low Mach numbers, between 10^{-1} and 10^{-4}. As shown in (Guillard and Viozat, 1999; LeMartelot et al., 2013), using Godunov-type scheme for low Mach number flows leads to large computational errors. A way to overcome this issue is to adapt a preconditioning technique, such as the one given in these references, to the present two-phase diffuse interface model.

As shown in (LeMartelot et al., 2013), it is mandatory to use an implicit scheme. For the sake of simplicity, the analysis is carried out in 2D.

The second issue concerns extra physics (surface tension, heat conduction and phase transition) numerical treatment. This issue will be addressed in the following subsections.

Implicit scheme

The system being hyperbolic, a Godunov type scheme is considered to solve System (21) in a Cartesian finite volume framework. A computational cell is schematized in Fig. 3. The implicit 2D Godunov scheme reads:

$$U_{ij}^{n+1} - U_{ij}^{n} = -\frac{\Delta t}{\Delta x}\left(F_{i+\frac{1}{2}j}^{n+1} - F_{i-\frac{1}{2}j}^{n+1}\right) - \frac{\Delta t}{\Delta y}\left(G_{ij+\frac{1}{2}}^{n+1} - G_{ij-\frac{1}{2}}^{n+1}\right) + \Delta t S_{ij}^{n+1}, \tag{24}$$

where

$$U = \begin{pmatrix} \rho Y_1 \\ \rho \\ \rho u \\ \rho v \\ \rho E \end{pmatrix} \quad F = \begin{pmatrix} \rho Y_1 u \\ \rho u \\ \rho u^2 + P \\ \rho vu \\ (\rho E + P)u \end{pmatrix} \quad G = \begin{pmatrix} \rho Y_1 v \\ \rho v \\ \rho uv \\ \rho v^2 + P \\ (\rho E + P)v \end{pmatrix}$$

$$S = \begin{pmatrix} 0 \\ 0 \\ \sigma\kappa\overrightarrow{\nabla Y_1}|_x + \rho\mathbf{g}|_x \\ \sigma\kappa\overrightarrow{\nabla Y_1}|_y + \rho\mathbf{g}|_y \\ -\operatorname{div}\left(\lambda_c \overrightarrow{\nabla T}\right) + \sigma\kappa\overrightarrow{\nabla Y_1} \bullet \mathbf{u} + \rho\mathbf{g} \bullet \mathbf{u} \end{pmatrix}.$$

The flux $F_{i+\frac{1}{2}j}^{n+1}, F_{i-\frac{1}{2}j}^{n+1}, G_{ij-\frac{1}{2}}^{n+1}, G_{i-j\frac{1}{2}}^{n+1}$ and "source" S_{ij}^{n+1} vectors are computed according to variables at time t^{n+1}. Let us consider a generic form of these vectors:

$$\Phi^{n+1} = \Phi^{n+1}\left(U_{ij}^{n+1}, U_{i-1j}^{n+1}, U_{i+1j}^{n+1}, U_{ij-1}^{n+1}, U_{ij+1}^{n+1}\right). \tag{25}$$

Under first order Taylor expansion it becomes

$$\begin{aligned}
\Phi^{n+1} = \Phi^{n} &+ \frac{\partial \Phi}{\partial U_{ij}}\Big)^n (U_{ij}^{n+1} - U_{ij}^{n}) + \frac{\partial \Phi}{\partial U_{i-1j}}\Big)^n (U_{i-1j}^{n+1} - U_{i-1j}^{n})\\
&+ \frac{\partial \Phi}{\partial U_{i+1j}}\Big)^n (U_{i+1j}^{n+1} - U_{i+1j}^{n}) + \frac{\partial \Phi}{\partial U_{ij-1}}\Big)^n (U_{ij-1}^{n+1} - U_{ij-1}^{n})\\
&+ \frac{\partial \Phi}{\partial U_{ij+1}}\Big)^n (U_{ij+1}^{n+1} - U_{ij+1}^{n}).
\end{aligned} \tag{26}$$

With the help of (26), Relation (24) becomes:

$$\begin{aligned}
&\left[I + \frac{\Delta t}{\Delta x}\left(\frac{\partial F_{i+\frac{1}{2}j}}{\partial U_{ij}}\right)^n - \frac{\partial F_{i-\frac{1}{2}j}}{\partial U_{ij}}\Big)^n\right) + \frac{\Delta t}{\Delta y}\left(\frac{\partial G_{ij+\frac{1}{2}}}{\partial U_{ij}}\right)^n - \frac{\partial G_{ij-\frac{1}{2}}}{\partial U_{ij}}\Big)^n\right)\\
&\quad + \Delta t\frac{\partial S_{ij}}{\partial U_{ij}}\Big)^n\Big]\delta U_{ij} + \frac{\Delta t}{\Delta x}\frac{\partial F_{i+\frac{1}{2}j}}{\partial U_{i+1j}}\Big)^n \delta U_{i+1j} - \frac{\Delta t}{\Delta x}\frac{\partial F_{i-\frac{1}{2}j}}{\partial U_{i-1j}}\Big)^n \delta U_{i-1j}\\
&\quad + \Delta t\left[\frac{\partial S_{ij}}{\partial U_{i-1j}}\Big)^n \delta U_{i-1j} + \frac{\partial S_{ij}}{\partial U_{i+1j}}\Big)^n \delta U_{i+1j}\right] + \frac{\Delta t}{\Delta y}\frac{\partial G_{ij+\frac{1}{2}}}{\partial U_{ij+1}}\Big)^n \delta U_{ij+1}\\
&\quad - \frac{\Delta t}{\Delta y}\frac{\partial G_{ij-\frac{1}{2}}}{\partial U_{ij-1}}\Big)^n \delta U_{ij-1} + \Delta t\left[\frac{\partial S_{ij}}{\partial U_{ij-1}}\Big)^n \delta U_{ij-1} + \frac{\partial S_{ij}}{\partial U_{ij+1}}\Big)^n \delta U_{ij+1}\right]\\
&= -\frac{\Delta t}{\Delta x}(F_{i+\frac{1}{2}j}^{n} - F_{i-\frac{1}{2}j}^{n}) - \frac{\Delta t}{\Delta y}(G_{ij+\frac{1}{2}}^{n} - G_{ij-\frac{1}{2}}^{n}) + \Delta t S_{ij}^{n},
\end{aligned} \tag{27}$$

where $\delta U_{ij} = U_{ij}^{n+1} - U_{ij}^{n}$.

Under compact form it reads: $M\delta U = D$ where M is a pentadiagonal sparse matrix. To optimise computations, the CSC (Saad, 1992) method, where only the non-zero elements are stored, is used.

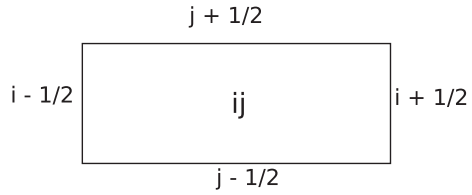

Fig. 3. Computational cell (i,j) bounded with its four cell boundaries, $(i+1/2,j)$, $(i-1/2,j)$, $(i,j+1/2)$ and $(i,j-1/2)$.

This system can be solved by either direct or iterative methods. In the present computations the PETSc (Balay et al., 2013a; Balay et al., 2013b; Balay et al., 1997) libraries are used.

Riemann solver

The various fluxes in System (24) are computed with the HLLC Riemann solver (Toro et al., 1994).

At cell boundary $i+\frac{1}{2}$, the flux F^* reads:

$$F^*_{L,R} = \frac{1}{2}(F_L + F_R) - sign(S_L)\frac{S_L}{2}(U^*_L - U_L) - sign(S_M)\frac{S_M}{2}(U^*_R - U^*_L) - sign(S_R)\frac{S_R}{2}(U_R - U^*_R), \quad (28)$$

with the same notations as previously for vectors U and F. The subscripts L and R denote the left and right states of the Riemann problem, respectively, as shown in Fig. 4.

The wave speeds S_R and S_L are estimated following Davis approximation (Davis, 1988),

$$S_R = Max(u_R + c_R, u_L + c_L), \quad (29)$$

$$S_L = Max(u_R - c_R, u_L - c_L), \quad (30)$$

while S_M is estimated under HLL (Harten et al., 1983) approximation:

$$S_M = \frac{S_R U_R(2) - S_L U_L(2) - (F_R(2) - F_L(2))}{S_R U_R(1) - S_L U_L(1) - (F_R(1) - F_L(1))}. \quad (31)$$

The states U^*_L and U^*_R in relation (28) are determined with the help of Rankine–Hugoniot jump relations across the S_R and S_L waves,

$$F^*_L - S_L U^*_L = F_L - S_L U_L, \quad (32)$$

$$F^*_R - S_R U^*_R = F_R - S_R U_R, \quad (33)$$

and with contact relations, $u^*_L = u^*_R = S_M$ and $P^*_L = P^*_R = P^*$:

$$U^*_L = \frac{1}{S_M - S_L}[F_L - S_L U_L - (0, P^*, S_M.P^*)^T] \quad (34)$$

$$U^*_R = \frac{1}{S_M - S_R}[F_R - S_R U_R - (0, P^*, S_M.P^*)^T] \quad (35)$$

The implicit Godunov scheme (27) requires the flux expression given by (28) and its derivatives with respect to the conservatives variables. Corresponding formulas are given in Appendix C.

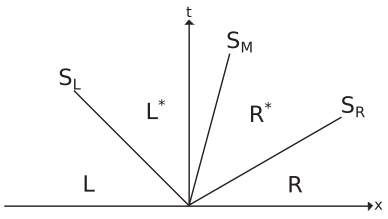

Fig. 4. Schematization of the System (21) Riemann problem under HLLC approximation in the absence of right hand sides (capillarity, relaxation and gravity effects).

Low Mach number preconditioning

As mentioned in the introduction, nucleate boiling flows involve compressible low Mach numbers flows. As shown in (Guillard and Viozat, 1999; LeMartelot et al., 2013), Godunov-type scheme leads to huge errors without appropriate correction. Following the lines of Turkel (1987) and Guillard and Viozat (1999) in the context of single phase flows, a multiphase flows preconditioning method is used. It consists in modifying the pressure equation associated with System Eq. (21):

$$\frac{\partial P}{\partial t} + u\frac{\partial P}{\partial x} + \rho c^2 \frac{\partial u}{\partial x} = 0, \quad (36)$$

by a M^2 factor,

$$\frac{1}{M^2}\frac{\partial P}{\partial t} + u\frac{\partial P}{\partial x} + \rho c^2 \frac{\partial u}{\partial x} = 0. \quad (37)$$

This modification leads to the modified wave speeds: $u, u+\tilde{c}_+, u-\tilde{c}_-$, with,

$$\tilde{c}_- = \frac{(1-M^2)u + \sqrt{(M^2-1)^2u^2 + 4M^2c^2}}{2}, \quad (38)$$

$$\tilde{c}_+ = \frac{(M^2-1)u + \sqrt{(M^2-1)^2u^2 + 4M^2c^2}}{2}, \quad (39)$$

which are directly used in the HLLC solver (28).

It is worth to mention that System (21) is only modified in the Riemann problem resolution through the wave speeds (38) and (39). With the fluxes computed thanks to the HLLC solver, the Godunov method (24) is used with formulation (21) and unmodified equation of state (17). This method obviously guarantees conservation and correct jumps across waves. It only acts on the numerical dissipation.

As the conservative formulation is used, even strong discontinuities can be handled by the method and, as shown in (LeMartelot et al., 2013), the method is time accurate. Nevertheless, as the artificial "sound speeds" (38, 39) tend to wrong values when M tends to 0, the following function is used at the discrete level:

$$M = \begin{cases} 1, & \text{if } M_i \geqslant 0.3 \\ M_i, & \text{if } 0.3 > M_i > M_{ref,min} \\ M_{ref,min}, & \text{if } M_i \leqslant M_{ref,min} \end{cases} \quad (40)$$

where M_i represents the local Mach number inside the i cell and $M_{ref,min}$ the minimum admissible Mach number. This minimum is typically of the order of 10^{-2}–10^{-3}.

Heat conduction

In this section, the calculation of the heat flux present in the total energy conservation equation is addressed. For the sake of simplicity the analysis is carried out in 1D.

The heat flux at the cell boundary are expressed as a function of T_i and T_{i+1} as:

$$q_{i+1/2} = -\frac{\lambda_{c,i}\lambda_{c,i+1}}{\lambda_{c,i} + \lambda_{c,i+1}}\frac{T_{i+1} - T_i}{\frac{1}{2}\Delta x}. \quad (41)$$

Therefore, the 1D numerical approximation of term div($\mathbf{q}$) for an i cell becomes:

$$\text{div}(\mathbf{q}) \simeq \frac{1}{\Delta x}\left(q^{n+1}_{i,i+1/2} - q^{n+1}_{i,i-1/2}\right). \quad (42)$$

The corresponding flux derivatives appearing in the implicit scheme (27) are given in Appendix D.

Surface tension computation

Surface tension effects are considered through the Continuum Surface Force (CSF) method of Brackbill et al. (1992). The capillary force is modelled as,

$$\mathbf{F}_\sigma = \sigma\kappa\overrightarrow{\nabla C} \tag{43}$$

where σ is the represents the surface tension coefficient (N m^{-1}), κ the represents the local curvature (m^{-1}), defined by $\kappa = -\text{div}\left(\frac{\overrightarrow{\nabla C}}{|\overrightarrow{\nabla C}|}\right)$, and C represents a colour function whose goal is to locate the interface separating the two phases.

In the present work, we use the mass fraction ($C = Y_1$) as colour function, as mass fractions are invariant across pressure waves. However, the numerical diffusion adds too much dissipation on the mass fraction (and too much numerical entropy to the system) to be used in the normal and curvature computations. It is thus necessary to restore the zero and one bounds in order to have the correct pressure jump across interfaces. Obviously, if the mesh was fine enough, the use of this extra variable could be avoided. Another way would be to use interface sharpening techniques (see, for example, Shukla et al. (2010)).

The colour function is reset using these rules:

$$\begin{cases} \text{If } C \geqslant 0.5, C = 1.0 \\ \text{Otherwise}, C = 0.0 \end{cases}$$

This provides a sharp profile for the colour function and accurate interface detection. Once the interface is localised, a diffusion operator is applied to the colour function, C, in order to obtain a smooth function (for the gradients calculation). In this work, a simple diffusion equation is considered:

$$\frac{\partial C}{\partial \tau} = D_{diff} \triangle C, \tag{44}$$

where D_{diff} is a diffusion coefficient (m^2 s^{-1}). D_{diff} and τ are chosen such as the colour function is diffused on about 4 cells.

Then, the gradients are computed with the following second order approximation:

$$\overrightarrow{\nabla C}_{ij} = \frac{(C_{i+1j} - C_{i-1j})}{2\Delta x}\cdot\vec{i} + \frac{(C_{ij+1} - C_{ij-1})}{2\Delta y}\cdot\vec{j}, \tag{45}$$

where $\vec{i}$ and $\vec{j}$ represent the unit vectors associated to the local 2D base.

Once the gradients are known, the curvature is computed. At the discrete level, the local curvature inside a given i cell is determined with the following expression:

$$\kappa_i = -\frac{1}{\Omega_i}\sum_{j\in V(i)}\widehat{n_{ij}}\cdot\overrightarrow{n_{ij}}\,l_{ij}, \tag{46}$$

where vectors $\widehat{n_{ij}}$ represent the normalised colour function gradients calculated between cells i and j, and Ω_i represents the volume of cell i. The vector $\overrightarrow{n_{ij}}$ represents the vector connecting the cell centres and l_{ij} the cell boundary length. A simple expression of the cell boundary interface normal vectors, $\widehat{n_{ij}}$, is given by:

$$\widehat{n_{ij}} = \frac{1}{2}(\hat{n}_j + \hat{n}_i), \tag{47}$$

where $\hat{n}_i = \frac{\overrightarrow{\nabla C}_i^n}{|\overrightarrow{\nabla C}_i^n|}$.

In the frame of 2D Cartesian grids it reduces to:

$$\kappa_{ij} = -\left(\frac{1}{\Delta x}(\hat{n}_{xi+\frac{1}{2}j} - \hat{n}_{xi-\frac{1}{2}j}) + \frac{1}{\Delta y}(\hat{n}_{yij+\frac{1}{2}} - \hat{n}_{yij-\frac{1}{2}})\right), \tag{48}$$

As for the previous convective and conductive fluxes, derivatives of the capillary term are needed. Details are given in Appendix E.

Validations

To check validity of the model, the numerical solution based on the diffuse interface model (21) is compared to a basic solution of one-dimensional sharp evaporation front. Then, capillary effects alone are considered in a 2D test case.

1D evaporation front

The goal of this section is to determine the exact solution of a 1D steady evaporation front in order to check convergence of the method presented previously.

We consider the following configuration (Fig. 5), with boundary conditions:

- Liquid inflow at imposed temperature, $T = T_{LI}$.
- Vapour outflow at imposed temperature, $T = T_{VO}$, with imposed heat flux, Q_0.

The stationary evaporation front is located at $x = 0$ and the corresponding temperature is equal to the liquid–gas saturation temperature, $T_{x=0} = T_{SAT}$.

The corresponding configuration is schematized in Fig. 5.

Reference solution determination

As the interface is considered as a sharp discontinuity, the single phase Euler equations with heat diffusion are valid in each pure fluid:

$$\begin{aligned} &\frac{\partial \rho}{\partial t} + \frac{\partial \rho u}{\partial x} = 0, \\ &\frac{\partial \rho u}{\partial t} + \frac{\partial \rho u^2 + P}{\partial x} = 0, \\ &\frac{\partial \rho E}{\partial t} + \frac{\partial (\rho E + P)u}{\partial x} - \frac{\partial}{\partial x}\left(\lambda\frac{\partial T}{\partial x}\right) = 0. \end{aligned} \tag{49}$$

Each phase is supposed to obey the stiffened-gas (3) equation of state, with discontinuous coefficients at the interface. As we consider steady state solution, System (49) reduces to:

$$\begin{aligned} &\rho\bar{u} = m = cst, \\ &\frac{m^2}{\rho_k} + P = cst, \\ &m\left(h_k + \frac{1}{2}\frac{m^2}{\rho_k^2} + q_k\right) - \lambda_k\frac{\partial T}{\partial x} = cst, \end{aligned} \tag{50}$$

where $\bar{u}$ represents the velocity in the evaporation front reference frame and $h_k = C_{p,k}T$ represents the thermal part of the enthalpy and q_k the reference enthalpy of phase k.

Quasi-isobar flow

By considering weak pressure variations, the pressure is considered as a constant at leading order, $P(x) = P_0$. This hypothesis, widely used in combustion theory (see Clavin and Garcia (1983),

Fig. 5. Geometry and boundary conditions.

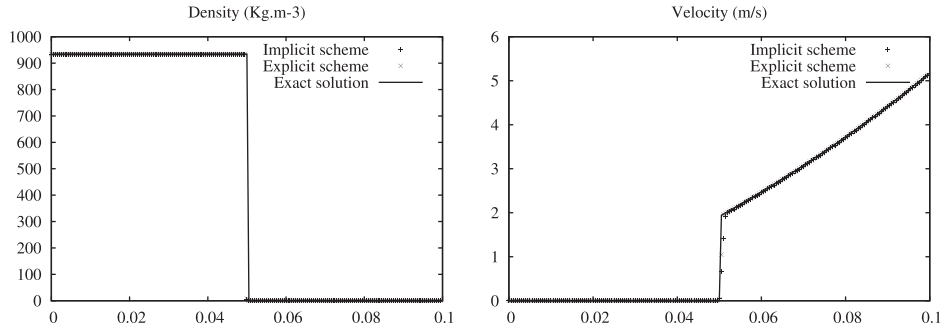

Fig. 6. Computed mixture density and velocity profiles using a mesh composed of 200 cells compared to the exact profiles. Excellent agreement is obtained.

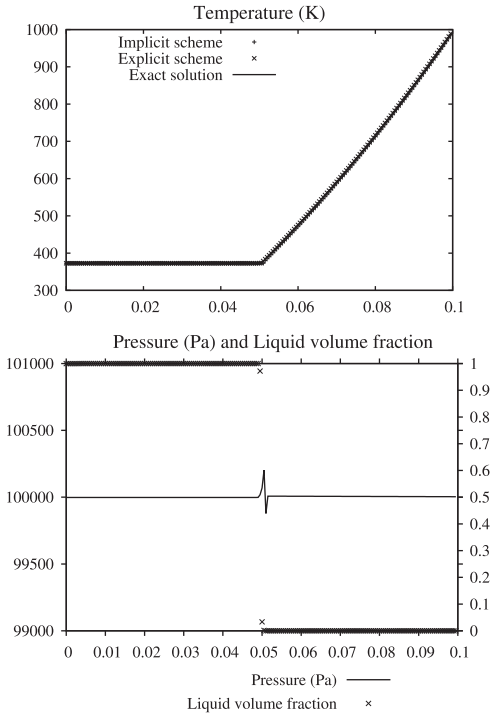

Fig. 7. Computed temperature, pressure and liquid volume fraction profiles using a mesh composed of 200 cells and the implicit scheme.

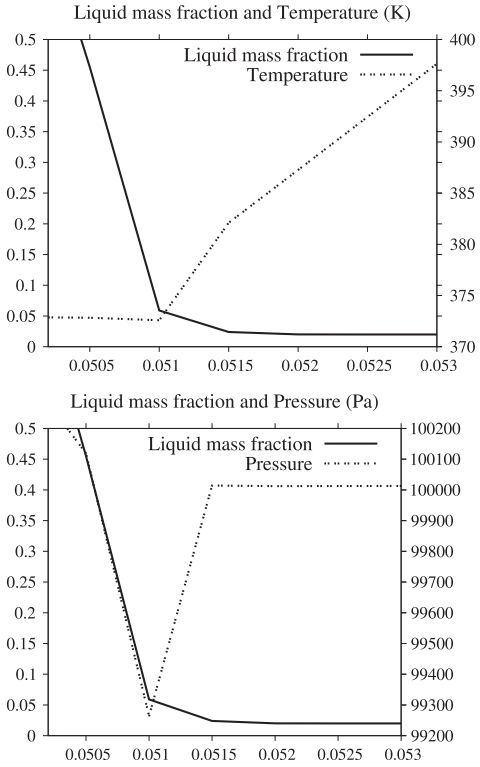

Fig. 8. Computed temperature, pressure and liquid mass fraction profiles using a mesh composed of 200 cells and the implicit scheme. Close up on the vapour side of the interface. The temperature being linked to the mass fraction, the pressure profile is modified accordingly in the areas where phase change is enabled.

for example) allows for the removal of the $\frac{1}{2}\frac{m^2}{\rho_k^2}$ term in the energy equation.

Therefore, total energy conservation expressed between the liquid inflow and the vapour outflow reads:

$$mC_{p,liq}T_{LI} + mq_{liq} = mC_{p,vap}T_{VO} + mq_{vap} + Q_0. \tag{51}$$

T_{LI} and T_{VO} being known, a first relation between the mass flow rate, m and the heat flux, $Q_0\left(Q_0 = -\lambda_{vap}\frac{\partial T}{\partial x}\right)_{x=X_V}$, is obtained:

$$Q_0 = m\left(C_{p,liq}T_{LI} + q_{liq} - C_{p,vap}T_{VO} - q_{vap}\right). \tag{52}$$

The temperature profiles on each side of the evaporation front are determined using the total energy conservation expressed between the inflow and a point inside each one of the pure fluid zones:

$$mC_{p,liq}T + mq_{liq} - \lambda_{liq}\frac{\partial T}{\partial x} = mC_{p,liq}T_{LI} + mq_{liq}, \tag{53}$$

$$mC_{p,vap}T + mq_{vap} - \lambda_{vap}\frac{\partial T}{\partial x} = mC_{p,liq}T_{LI} + mq_{liq}, \tag{54}$$

with the help of the interface condition $T_{x=0} = T_{SAT}$, the following solutions are obtained:

$$\begin{aligned} T(x)|_{x<0} &= T_{LI} + (T_{SAT} - T_{LI})e^{\frac{mC_{p,liq}}{\lambda_{liq}}x}, \\ T(x)|_{x>0} &= \frac{C_{p,liq}}{C_{p,vap}}T_{LI} + \frac{q_{liq} - q_{vap}}{C_{p,vap}} + \left(T_{SAT} - \frac{C_{p,liq}}{C_{p,vap}}T_{LI} - \frac{q_{liq} - q_{vap}}{C_{p,vap}}\right)e^{\frac{mC_{p,vap}}{\lambda_{vap}}x}. \end{aligned} \tag{55}$$

In order to determine the mass flux, m, another relation linking m and Q_0 is needed. The heat flux definition at the outlet is used:

$$\begin{aligned} Q_0 &= -\lambda_{vap}\frac{\partial T}{\partial x}\Big)_{x=X_V}, \\ Q_0 &= -mC_{p,vap}\left(T_{SAT} - \frac{C_{p,liq}}{C_{p,vap}}T_{LI} - \frac{q_{liq} - q_{vap}}{C_{p,vap}}\right)e^{\frac{mC_{p,vap}}{\lambda_{vap}}X_V}. \end{aligned} \tag{56}$$

Using relations (52) and (56), the mass flow rate is determined as:

$$m = \frac{\lambda_{vap}}{C_{p,vap} L_V} \ln\left(\frac{C_{p,vap} T_{VO} + q_{vap} - C_{p,liq} T_{LI} - q_{liq}}{C_{p,vap} T_{SAT} + q_{vap} - C_{p,liq} T_{LI} - q_{liq}}\right). \quad (57)$$

Then, Q_0 is determined with (52).

Numerical solution

We consider the same test case as depicted in Fig. 5 with $T_{LI} = T_{SAT} = 372.79$ K, $T_{VO} = 1000$ K, $P(x) = P_0 = 1$ Bar, and the two following fluids:

Liquid:

$\gamma_{liq} = 2.62 \quad P_{\infty,liq} = 9058.29 \times 10^5$ Pa $\quad C_{v,liq} = 1606.97$ J kg^{-1} K^{-1}

$q_{liq} = -1.150975 \times 10^6$ J $\quad \lambda_{liq} = 0.6788$ W m^{-1} K^{-1}

Vapour:

$\gamma_{vap} = 1.38 \quad P_{\infty,vap} = 0$ Pa $\quad C_{v,vap} = 1192.51$ J kg^{-1} K^{-1}

$q_{vap} = 2.060759 \times 10^6$ J $\quad \lambda_{vap} = 249.97$ W m^{-1} K^{-1}

The vapour is considered as an ideal gas, even if its temperature may be supercritical. Indeed, at atmosphere pressure and with such high temperature, the density of the vapour is low and the ideal gas assumption is valid. Using the quasi-isobar analytical solution, the mass flow rate and the heat flux at the outlet are determined:

$m = 1.1434$ kg m^{-2} s^{-1} $\quad Q_0 = -3.76 \times 10^6$ W m^{-2}

The diffuse interface model is now considered. In 1D it reads,

$$\begin{aligned}
&\frac{\partial \rho Y_1}{\partial t} + \frac{\partial \rho Y_1 u}{\partial x} = \rho v (g_2 - g_1),\\
&\frac{\partial \rho}{\partial t} + \frac{\partial \rho u}{\partial x} = 0,\\
&\frac{\partial \rho u}{\partial t} + \frac{\partial \rho u^2 + P}{\partial x} = 0,\\
&\frac{\partial \rho E}{\partial t} + \frac{\partial (\rho E + P) u}{\partial x} = -\frac{\partial}{\partial x}(\lambda_c \frac{\partial T}{\partial x}).
\end{aligned} \quad (58)$$

It is solved numerically with the algorithm presented previously.

The boundary condition at the left inlet corresponds to an imposed mass flow rate and stagnation enthalpy, computed with the following set of variables:

$m = 1.1434$ kg m^{-2} s^{-1}, $\quad T = T_{SAT} = 372.79$ K,
$P = 1.0$ Bar, $\quad \alpha_{liq} = 0.999999$.

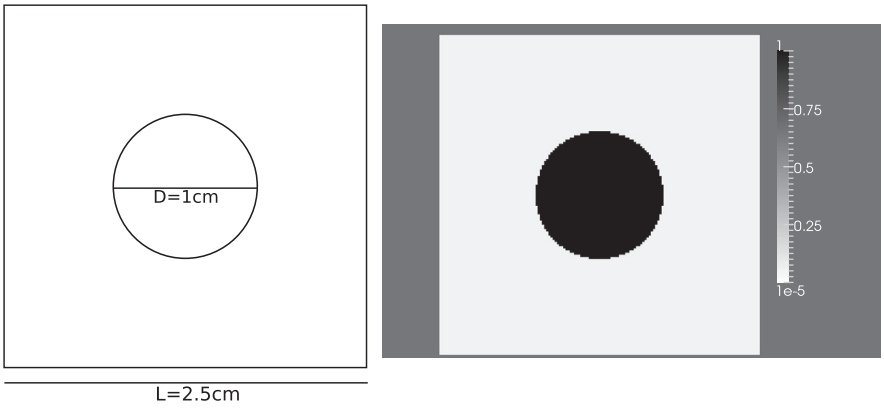

Fig. 9. Square domain filled with liquid water containing a incondensable gas bubble. Sketch of the configuration and initial volume fraction contours.

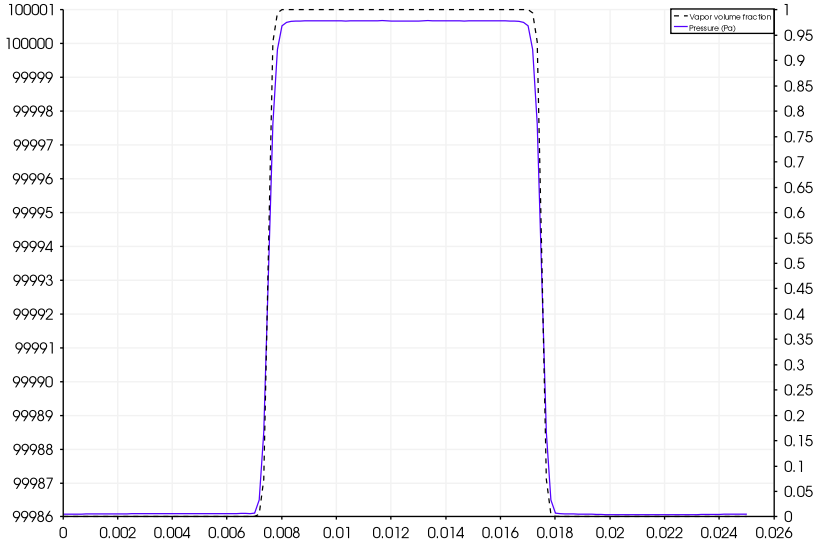

Fig. 10. Pressure and gas volume fraction profiles along the x-axis. The solid line represents the pressure while the dashed line represents the vapour volume fraction.

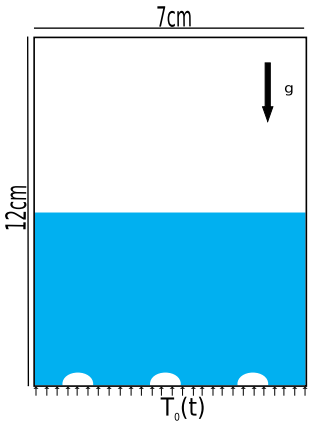

Fig. 11. A closed and adiabatic rectangular domain is considered. The lower half domain is filled with liquid water and the upper half is filled with water vapour. Three half vapour bubbles (radius = 3 mm) are initially present. A time dependent temperature, $T_0(t)$, is imposed at the bottom wall.

At the outlet boundary condition, the heat flux is prescribed as well as the pressure:

$$Q_0 = -3.76.10^6 \text{ W m}^{-2}, \quad P_0 = 1 \text{ Bar}.$$

This quite huge heat flux is due to the chosen value for the gas thermal conductivity (249.97 W m^{-1} K^{-1}). Indeed, the goal of these computations is to prove the ability of the method to converge to a solution with a sharp evaporating interface. Therefore, this conductivity has been chosen in order to lower the computational time required to converge to the exact solution. Another option could be to set the liquid gas interface close to the outlet section, but this is less convenient for both computations and representation of the results.

The numerical solution has been computed using both the explicit and the implicit (27) schemes on a mesh containing 200 cells. The numerical results compared to the exact solution are shown in Figs. 6 and 7. The peaks visible in the pressure graph are due to the numerical diffusion of mass fractions. Indeed, as we consider a model having a thermodynamics with coupled pressure–temperature and mass fraction, the temperature is strongly linked to the mass fraction (as shown in Relation (12) at a given pressure). Therefore, the temperature changes inside the diffusion zone, leading to a monotonic increasing profile inside this zone. However, as heat and mass transfer are considered, the pressure is also linked to the temperature in the cells where heat and mass transfer is enabled (as explained in Appendix B).

Thus, pressure peaks appear on each side of the interface as a consequence of heat diffusion and liquid mass consumption. This behaviour is illustrated in Fig. 8, showing a close up of the pressure and temperature profiles with the liquid mass fraction profile, on the right side of the interface.

Overall, these results show the ability of the method to converge to the exact 1D steady solution having a sharp evaporating interface. Therefore, it gives a first validation of the model.

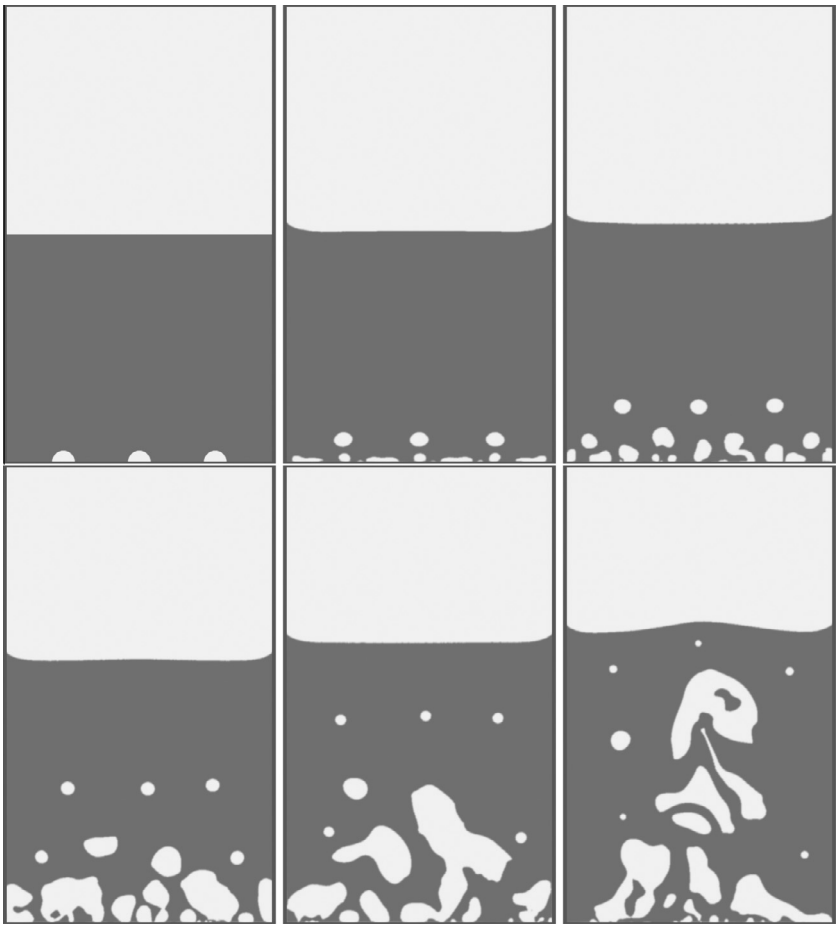

Fig. 12. Colour function at times $t = 0$ s, $t = 50$ ms, $t = 100$ ms, $t = 200$ ms, $t = 300$ ms and $t = 400$ ms. The three first bubbles are moving toward the surface due to buoyancy but, as the bottom of the box is heated, the water around them begins to boil and a vapour film appears. It forms new bubbles which begin to rise as new ones appear behind them.

Laplace law

We consider a closed squared domain of 2.5×2.5 cm filled with liquid water. A gas bubble (radius = 5 mm) is set at the centre (Fig. 9). Initially, the pressure and the temperature are set equal to 1Bar and 300 K everywhere while the volume fraction of vapour inside the bubble is 0.99999 and 10^{-5} outside. The surface tension coefficient is $\sigma = 73 \times 10^{-3}$ N m^{-1}. Low Mach pre-conditioning (see section 'Low Mach number preconditioning') is used with a reference Mach number equal to 0.1. The fluids SG EOS (3) parameters are the following:

Liquid:

$$\gamma_{liq} = 2.62 \quad P_{\infty,liq} = 9058.29 \times 10^5 \text{ Pa} \quad C_{v,liq} = 1606.97 \text{ J Kg}^{-1} \text{ K}^{-1}$$

Gas:

$$\gamma_{gas} = 1.38 \quad P_{\infty,gas} = 0 \text{ Pa} \quad C_{v,gas} = 1192.51 \text{ J Kg}^{-1} \text{ K}^{-1}$$

The C_v parameter is required in this computation as the temperature equilibrium model (6) (without mass transfer) is used. Fig. 10 shows the equilibrium state obtained on a 2D grid composed of 125×125 cells.

These results allow the determination of the numerical pressure jump, $(\Delta P)_{num} \simeq 14.9$ Pa, which is to be compared to the Laplace's law, $\Delta P = \frac{\sigma}{0.5D} = \frac{73 \times 10^{-3}}{0.005} = 14.6$ Pa.

Therefore, the obtained pressure jump is in good agreement with the exact solution, with an error of about 2.05%.

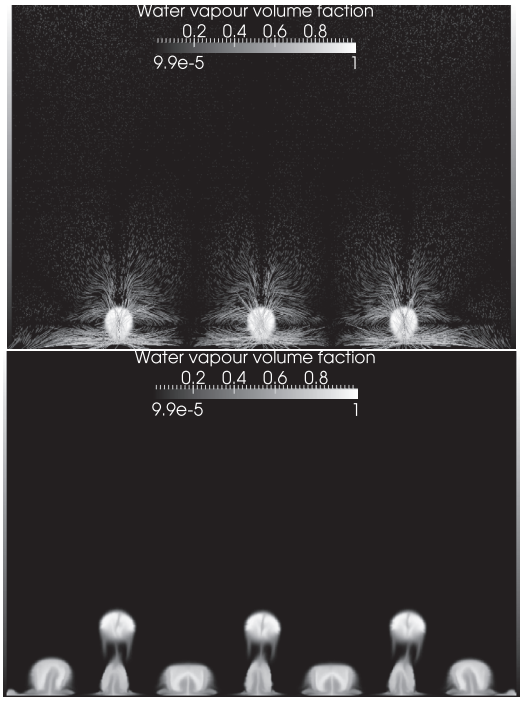

Fig. 14. Water vapour volume fraction and velocity vectors around the bubbles at time $t = 30$ ms and water vapour volume fraction at time $t = 70$ ms.

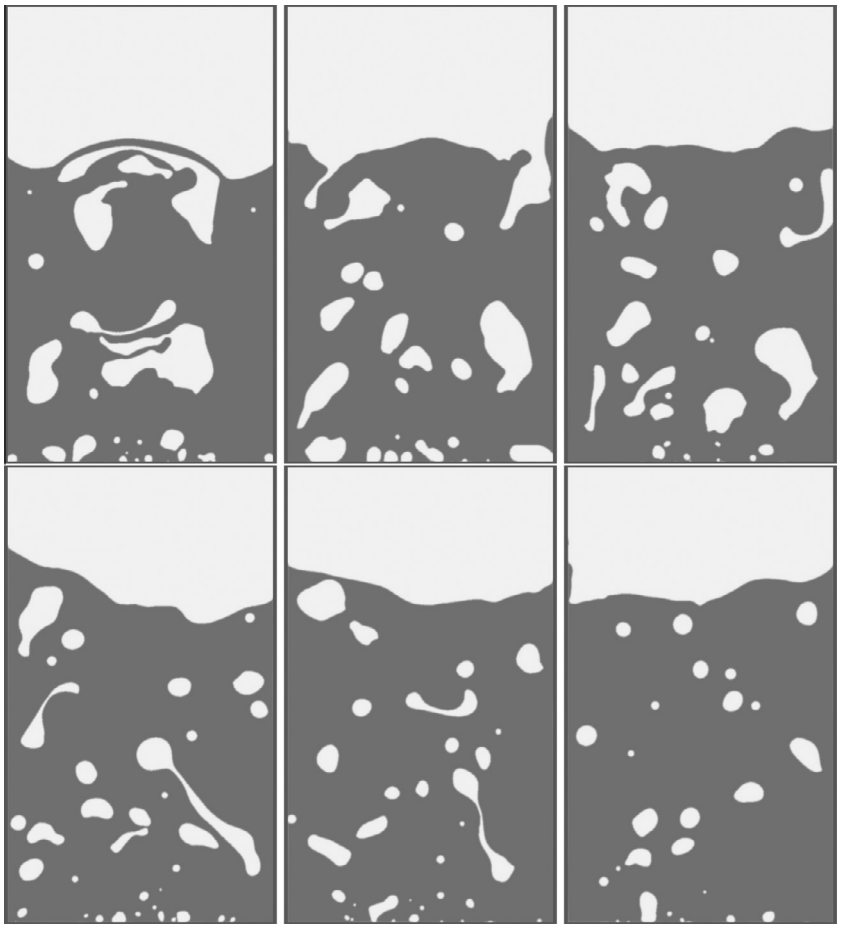

Fig. 13. Colour function at times $t = 500$ ms, $t = 600$ ms, $t = 700$ ms, $t = 800$ ms, $t = 900$ ms and $t = 1000$ ms. New bubbles continue to rise as the first ones begin the interact with the liquid–vapour upper surface. The bottom of the box being a perfect surface, the new bubbles are created at different positions than the initial sites, meaning that their position and size is selected by convection, conduction and capillarity.

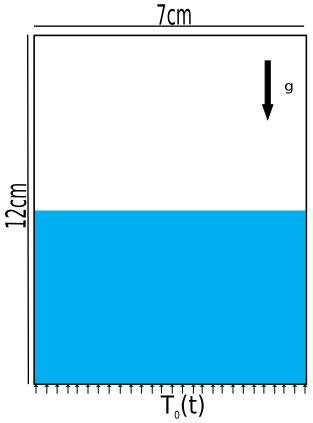

Fig. 15. A closed and adiabatic rectangular domain is considered. The lower half domain is filled with liquid water and the upper half is filled with water vapour. A temperature, $T_0(t)$, is imposed at the bottom wall.

In order to check the method convergence, the same test has been done with a finer grid (250×250). This time, the pressure jump is 14.7 Pa, which corresponds to an error of about 0.68%.

2D illustrations

The aim of this section is to show capabilities of the model when all physical effects present in System (21) are considered.

A closed and adiabatic rectangular domain (12×7 cm) in which the lower half is filled with saturated liquid water and the upper half is filled with saturated vapour is considered. Then, the behaviour of a boiling flow inside this domain is studied.

The surface tension coefficient is set to $\sigma = 73 \times 10^{-3}$ N m^{-1}, the contact angle is taken constant and equal to $\theta = 45^\circ$ and the gravity acceleration is set to $|\mathbf{g}| = 9.81$ m s^{-2}. The fluid parameters are the following:

Liquid water:

$$\gamma_{liq} = 2.62 \quad P_{\infty,liq} = 9058.29 \times 10^5 \text{ Pa} \quad C_{v,liq} = 1606.97 \text{ J kg}^{-1} \text{ K}^{-1}$$

$$q_{liq} = -1.150975 \times 10^6 \text{ J} \quad \lambda_{liq} = 0.6788 \text{ W m}^{-1} \text{ K}^{-1}$$

Water vapour:

$$\gamma_{vap} = 1.38 \quad P_{\infty,vap} = 0 \text{ Pa} \quad C_{v,vap} = 1192.51 \text{ J kg}^{-1} \text{ K}^{-1}$$

$$q_{vap} = 2.060759 \times 10^6 \text{ J} \quad \lambda_{vap} = 0.0249 \text{ W m}^{-1} \text{ K}^{-1}$$

At start, the initial volume fraction of vapour is $\alpha_{vap} = 0.0001$ in the lower half domain and $\alpha_{vap} = 0.9999$ in the upper part. Moreover, the initial pressure and temperature are initialised with the hydrostatic gravity profile with the constraint $T = T_{SAT}(P)$ in each cell. A time dependent temperature, $T_0(t)$, is imposed at the bottom wall such as:

$$T_0(t) = \begin{cases} T_{SAT} + \left(\frac{t}{\tau}\right)\Delta T, & \text{if } t \leqslant \tau \\ T_{SAT} + \Delta T, & \text{if } t > \tau \end{cases} \tag{59}$$

with $\tau = 150$ ms, $T_{SAT} = 372.79$ K and $\Delta T = 15$ K. This smooth heating is set in order to avoid creation of a vapour film along the hot surface and too strong pressure waves.

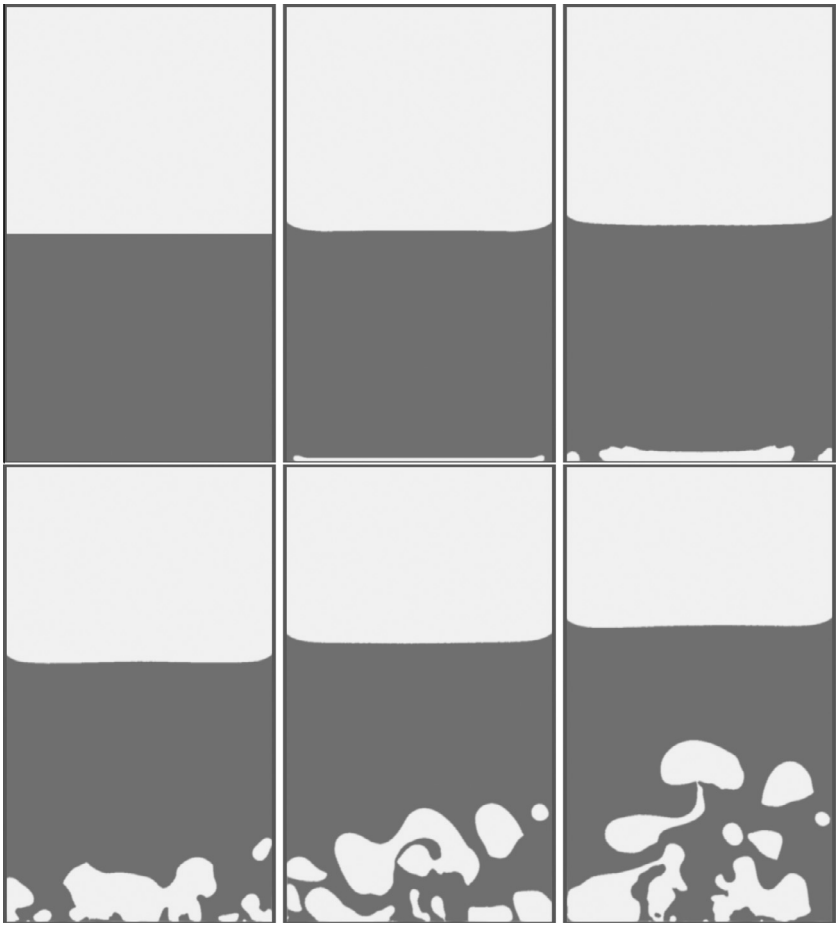

Fig. 16. Colour function at times $t = 0$ s, $t = 50$ ms, $t = 100$ ms, $t = 200$ ms, $t = 300$ ms and $t = 400$ ms. The first instants show the creation of a vapour film. As a result of wall effects a big elongated vapour bubble is created at the centre then breaks up into several bubbles. New bubbles appear at the bottom wall as a consequence of wall heating.

The behaviour of boiling flows is studied through two sets of initial conditions. First, three vapour bubbles are initially present at the bottom of the box (Fig. 11). Second, the same case is considered without these bubbles (Fig. 15).

The implicit scheme (27) and low Mach pre-conditioning are used with a mesh composed of 960×560 cells.

Boiling flow with vapour bubbles initially present

We consider the test case presented in the previous section with three vapour bubbles (radius = 3 mm) initially present. The volume fraction of vapour inside these bubbles is $\alpha_{vap} = 0.9999$ (Fig. 11). The computed colour function is shown in Figs. 12 and 13. The colour function is computed as detailed in Section 'Surface tension computation'.

The first instants show the three first bubbles moving toward the surface due to buoyancy effects while, as the bottom wall of the box is heated, water around begins to boil, creating a vapour film. The boiling phenomenon appears as consequence of wall heating effect that renders the liquid locally slightly overheated. Indeed, the assumption made is that the liquid contains enough impurities to not accept overheating, as pure liquids are able to become metastable while real liquids are not. Therefore, using the phase transition solver of Appendix B, after checking that the liquid is not in stable state (Eqs. 63 and 64), the equilibrium state is computed with System (66) and a mixed cell appears. From this "nucleation cell site" and merging effects due to surface tension, convection and inertia, new bubbles appear. Once created, theses new bubbles begin to rise and, as there is now again liquid in contact with the bottom wall, new bubbles appear behind them and begin to grow.

It is worth to mention that the bottom wall of the box is a perfect surface, exempt of cavities or special treatment except for uniform temperature and constant contact angle. According to the velocity profiles, the first bubbles seem to be created between the convective rolls, where the velocity is the lowest, as shown in Fig. 14.

These results tend to indicate that heterogeneous nucleation at walls helps the boiling phenomenon but is not mandatory if the liquid cannot remain metastable. In this case, each time a portion of liquid is overheated, a nucleus is created. This nucleus grows and merge with other nuclei to dynamically form bubbles. The flow model does not need nucleation criterion, except rejection of metastable states, which is commonly accepted with real liquids. The phenomenon is then self-sustained and selects the number of bubbles and their sizes. To check pertinence of this scenario, we consider, in the next section, the same test case but without vapour bubbles initially present.

Boiling flow without vapour bubbles initially present

The same test case as previously is considered in the absence of initial nucleation sites (Fig. 15). The colour function is shown in Figs. 16 and 17.

The first instants show the creation of a vapour film. As a result of surface tension, wall effects appear and a big elongated vapour bubble is created at the centre. Then, convective effects created by the first bubble combined with surface tension effects, create new bubbles at the bottom wall. Once created, theses new bubbles

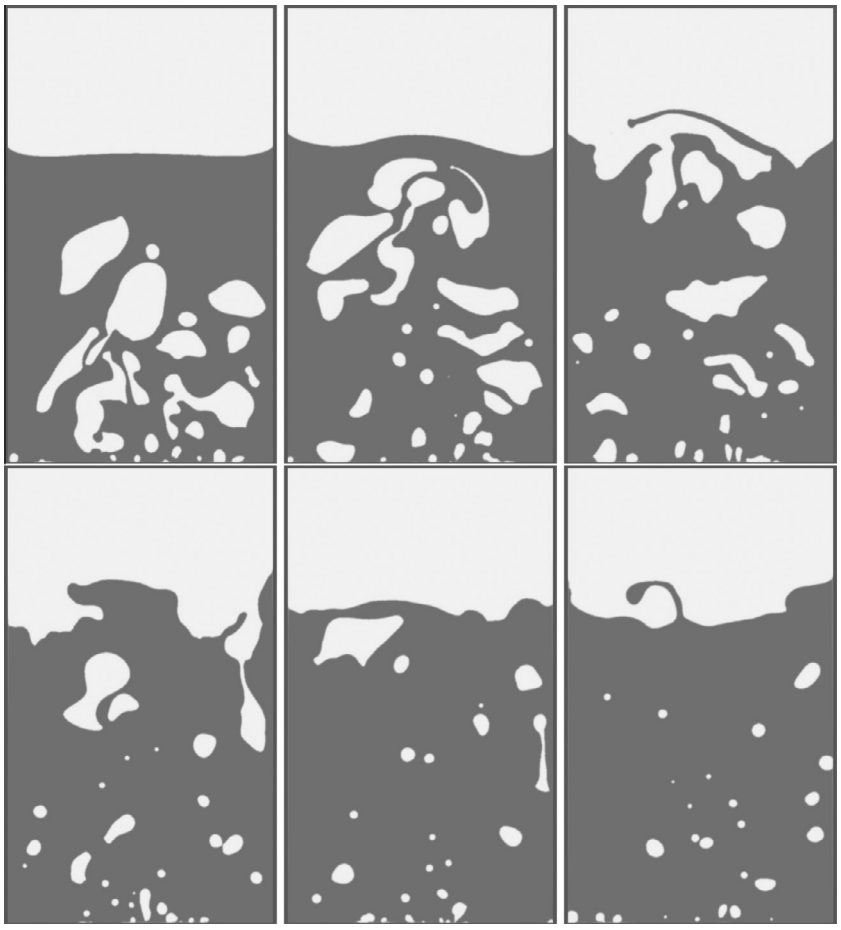

Fig. 17. Colour function at times $t = 500$ ms, $t = 600$ ms, $t = 700$ ms, $t = 800$ ms, $t = 900$ ms and $t = 1000$ ms. Newly created bubbles continue to rise as the first ones begin to interact with the surface.

begin to rise and, as there is now again liquid in contact with the bottom wall, new ones appear behind them and begin to grow.

These results show that boiling phenomenon, and consequently the associated flow model, may not require heterogeneous nucleation. Moreover, qualitatively, the nucleation bubbles size selection as well as the way the bubbles rise are very similar to the previous case, where nucleation sites are initially present, consolidating the previous observations.

Conclusion

As a first step towards the direct numerical simulation of nucleate boiling flows, a thermal and mechanical equilibrium model has been built. This model considers fluids compressibility, is hyperbolic and in agreement with the second law of thermodynamics. Moreover, it has no restriction regarding interfacial density, pressure ratios as well as flow speed. Extra physics (surface tension Brackbill et al. (1992), gravity, heat conduction and phase change Saurel et al. (2008) and Le Métayer et al. (2004)) has been added to the model. Nevertheless, as boiling flows involve compressible low Mach numbers conditions, a preconditioning method (Turkel, 1987; Guillard and Viozat, 1999) with an implicit scheme (LeMartelot et al., 2013) has been adapted to the present model to obtain accurate solutions.

The method has been validated against 1D steady sharp evaporation front exact solution and a 2D static bubble case, showing agreement with Laplace's law.

Two-dimensional nucleate boiling flow simulations have been addressed. The corresponding results show very good qualitative behaviour as well as the ability of the method to deal with such complex flows.

Acknowledgments

The first author has been partly supported by CNES and SAFRAN Snecma, space Engines Division. Drs. S. Petitot and P. Boivin are gratefully acknowledged. The authors would like to acknowledge fruitful discussions and works with Drs. F. Petitpas and O. Le Metayer.

They also gratefully acknowledge the Referees for the pertinence and deepness of their analyses, that helped manuscript improvement. This work has been carried out in the framework of the Labex MEC (ANR-10-LABX-0092) and A*MIDEX Project (ANR-11-iDEX-0001-02) funded by "Investissements d'Avenir", French Government program managed by the French National Research Agency (ANR).

Appendix A. Heat conduction insertion in the reduced model

To insert conductive effects in System (6) a two-phase flow model in total non-equilibrium is considered:

$$
\begin{aligned}
&\frac{\partial \alpha_1}{\partial t} + \mathbf{u}_1 \bullet \mathbf{grad}(\alpha_1) = \mu(p_1 - p_2),\\
&\frac{\partial \alpha_1\rho_1}{\partial t} + \mathrm{div}(\alpha_1\rho_1\mathbf{u}_1) = 0,\\
&\frac{\partial (\alpha\rho\mathbf{u})_1}{\partial t} + \mathrm{div}(\alpha\rho\mathbf{u}\otimes\mathbf{u} + \alpha p)_1 = P_I\nabla\alpha_1 + \lambda(u_2 - u_1),\\
&\frac{\partial (\alpha\rho E)_1}{\partial t} + \mathrm{div}(\alpha(\rho E + p)\mathbf{u} + \alpha\mathbf{q})_1 = (P_I u_I + \mathbf{q}_I)\nabla\alpha_1 + \lambda u_I'(u_2 - u_1)\\
&\qquad\qquad - \mu P_I'(p_1 - p_2) + H(T_2 - T_1),\\
&\frac{\partial \alpha_2\rho_2}{\partial t} + \mathrm{div}(\alpha_2\rho_2\mathbf{u}_2) = 0,\\
&\frac{\partial (\alpha\rho\mathbf{u})_2}{\partial t} + \mathrm{div}(\alpha\rho\mathbf{u}\otimes\mathbf{u} + \alpha p)_2 = P_I\nabla\alpha_2 - \lambda(u_2 - u_1),\\
&\frac{\partial (\alpha\rho E)_2}{\partial t} + \mathrm{div}(\alpha(\rho E + p)\mathbf{u} + \alpha\mathbf{q})_2\\
&\quad = (P_I u_I + \mathbf{q}_I)\nabla\alpha_2 - \lambda u_I'(u_2 - u_1) + \mu P_I'(p_1 - p_2) - H(T_2 - T_1).
\end{aligned}
\tag{60}
$$

The precise expressions for the interfacial variables P_I, u_I and heat flux $\mathbf{q}_I$ are useless as well as the precise expressions for the various relaxation parameters (μ (pressure relaxation), λ (velocity relaxation) and H (temperature relaxation)). Indeed, the limit model when these relaxation effects are stiff is under interest. In other words, an asymptotic analysis can be carried out in the limit of stiff mechanical and thermal relaxation.

For each flow variable f an asymptotic expansion, $f = f^0 + \epsilon f^1$ is considered. f^0 representing the equilibrium state and f^1 a small perturbation. Furthermore, each relaxation coefficient (μ, λ and H) is supposed stiff:

$$
\mu = \frac{\mu_0}{\epsilon}, \lambda = \frac{\lambda_0}{\epsilon}, H = \frac{H_0}{\epsilon} \tag{61}
$$

where $\epsilon \to 0$

In this limit, the leading order system corresponds to the extension of System (6) with heat conduction effects:

$$
\begin{aligned}
&\frac{\partial \rho Y_1}{\partial t} + \mathrm{div}(\rho Y_1\mathbf{u}) = 0,\\
&\frac{\partial \rho}{\partial t} + \mathrm{div}(\rho\mathbf{u}) = 0,\\
&\frac{\partial \rho\mathbf{u}}{\partial t} + \mathrm{div}(\rho\mathbf{u}\otimes\mathbf{u} + P) = 0,\\
&\frac{\partial \rho E}{\partial t} + \mathrm{div}((\rho E + P)\mathbf{u}) + \mathrm{div}(\mathbf{q}) = 0,
\end{aligned}
\tag{62}
$$

where $\mathbf{q} = -\lambda_c\overrightarrow{\nabla T}$ and $\lambda_c = \alpha_1\lambda_1 + \alpha_2\lambda_2$. λ_c represents the mixture thermal conductivity, λ_k represents the thermal conductivity of phase k and T the temperature.

Appendix B. Phase transition solver

The diffuse interface model given by System (6) corresponds to a multiphase description of a flow mixture evolving in mechanical and thermal equilibrium but out of thermodynamic equilibrium. Phase transition is handled through a stiff Gibbs free energies relaxation solver. This solver is used everywhere inside the calculation domain as it considers pure liquid and pure gas existence as well as liquid–gas mixture existence at interfaces, when phase change is expected. However, if the thermodynamic equilibrium state corresponds to total evaporation (pure vapour) or total condensation (pure liquid), the thermodynamic equilibrium relaxation solver should not be used. Thus, we first check this condition.

In each cell, the saturation temperature, $T_{SAT}(P)$ is calculated using the mixture pressure. Then, the saturated volumes of each phase can be determined:

$$
\begin{aligned}
&v_{liq,sat} = \frac{(\gamma_{liq} - 1)C_{v,liq}T_{SAT}}{P + P_{\infty,liq}},\\
&v_{vap,sat} = \frac{(\gamma_{vap} - 1)C_{v,vap}T_{SAT}}{P}.
\end{aligned}
\tag{63}
$$

These two volumes determine the saturation dome boundaries for the pressure/temperature couple $(P, T_{SAT}(P))$. Therefore, phase change can only happen if

$$
v_{liq,sat} < v < v_{vap,sat}, \tag{64}
$$

where v represents the mixture specific volume.

Thus, if this condition is fulfilled, it means that a two-phase mixture is present. In this case, the thermodynamic equilibrium condition,

$$
g_{liq})_I = g_{vap})_I, \tag{65}
$$

has to be fulfilled. If it is not, the state is unchanged.

If the computational cell contains a two-phase mixture, the corresponding algebraic system to solve reads:

$\rho = \alpha_{liq}\rho_{liq} + \alpha_{vap}\rho_{vap}$ or alternatively $v = \frac{1}{\rho} = Y_{liq}v_{liq} + Y_{vap}v_{vap}$,
$e = Y_{liq}e_{liq} + Y_{vap}e_{vap}$,
$T_{liq} = T_{vap} = T$,
$p_{liq} = p_{vap} = P$,
$g_{liq} = g_{vap}$. (66)

In order to avoid numerical issues related to time integration of stiff differential equations, when v (appearing in System (6)) tends to infinity, the thermodynamic equilibrium state of (66) is determined by the method that follows.

The specific volumes and the internal energies of each phase are expressed as functions of the pressure and temperature by (11) and (14). Each parameter involved in these expressions $(\gamma_k, C_{v,k}, P_{\infty,k}, q_k)$ is calculated in order to fit the liquid–vapour phase diagram, more precisely the corresponding saturation curves. Details regarding the EOS parameters determination are given in (Le Métayer et al., 2004; Saurel et al., 2008).

Denoting the relaxed state solution of System (66) by the superscript '$*$', the mass conservation constraint becomes,

$$\begin{aligned} v_0 &= Y^*_{liq}v^*_{liq}(P^*) + Y^*_{vap}v^*_{vap}(P^*) \\ &= Y^*_{liq}v^*_{liq}(P^*) + (1 - Y^*_{liq})v^*_{vap}(P^*), \end{aligned} \tag{67}$$

where $v^*_k(P^*) = v_k(P^*, T^*)$.

Constraints of pressures, temperatures and Gibbs free energies equalities result in,

$$T^*(P^*) = T_{SAT}(P^*). \tag{68}$$

Therefore the specific volumes, $v^*_{liq}(P^*)$ and $v^*_{vap}(P^*)$, become function of the pressure only. A first relation linking the liquid mass fraction and the pressure is thus obtained,

$$Y^*_{liq} = \frac{v^*_{vap}(P^*) - v_0}{v^*_{vap}(P^*) - v^*_{liq}(P^*)}. \tag{69}$$

As the kinetic energy is constant, the mixture total energy definition reads:

$$\begin{aligned} e_0 &= Y^*_{liq}e^*_{liq}(P^*) + Y^*_{vap}e^*_{vap}(P^*) \\ &= Y^*_{liq}e^*_{liq}(P^*) + (1 - Y^*_{liq})e^*_{vap}(P^*). \end{aligned} \tag{70}$$

A second relation linking the liquid mass fraction and the pressure is thus obtained,

$$Y^*_{liq} = \frac{e_0 - e^*_{vap}(P^*)}{e^*_{liq}(P^*) - e^*_{vap}(P^*)}. \tag{71}$$

This relation can be also expressed as a function of the specific enthalpies of the phases,

$$Y^*_{liq} = \frac{h^*_{vap}(p^*) - (e_0 - P^*v_0)}{h^*_{vap}(P^*) - h^*_{liq}(P^*)}, \tag{72}$$

where h_{liq} and h_{vap} are linked by $h^*_{vap}(P^*) - h^*_{liq}(P^*) = L_v(P^*), L_v(P^*)$ representing the latent heat of vapourization, which is a function of the pressure.

From the previous mass fraction equations, a single function of the pressure is obtained,

$$\frac{h^*_{vap}(P^*) - (e_0 - P^*v_0)}{h^*_{vap}(P^*) - h^*_{liq}(P^*)} - \frac{v^*_{vap}(P^*) - v_0}{v^*_{vap}(P^*) - v^*_{liq}(P^*)} = 0. \tag{73}$$

Its solution is computed with the Newton method. Existence and uniqueness of the solution when $0 < Y^*_{liq} < 1$ has been proved in (Allaire et al., 2007).

Once the relaxed pressure is determined, the remaining variables are easily computed with the preceding thermodynamic relations.

Appendix C. HLLC Riemann solver derivatives

The HLLC approximate Riemann solver is recalled hereafter:

$$\begin{aligned} F_{LR} = \frac{1}{2}(F_L + F_R) &- sign(S_L)\frac{S_L}{2}(U^*_L - U_L) - sign(S_M)\frac{S_M}{2}(U^*_R - U^*_L) \\ &- sign(S_R)\frac{S_R}{2}(U_R - U^*_R). \end{aligned}$$

The flux vector derivatives are given by:

$$\begin{aligned} \frac{\partial F_{LR}}{\partial U_L} = \frac{1}{2}\frac{\partial F_L}{\partial U_L} &- sign(S_L)\frac{S_L}{2}\left(\frac{\partial U^*_L}{\partial U_L} - 1\right) - sign(S_M)\frac{S_M}{2}\left(\frac{\partial (U^*_R - U^*_L)}{\partial U_L}\right) \\ &+ sign(S_R)\frac{S_R}{2}\left(\frac{\partial U^*_R}{\partial U_L}\right), \end{aligned} \tag{74}$$

$$\begin{aligned} \frac{\partial F_{LR}}{\partial U_R} = \frac{1}{2}\frac{\partial F_R}{\partial U_R} &- sign(S_L)\frac{S_L}{2}\frac{\partial U^*_L}{\partial U_R} - sign(S_M)\frac{S_M}{2}\left(\frac{\partial (U^*_R - U^*_L)}{\partial U_R}\right) \\ &- sign(S_R)\frac{S_R}{2}\left(1 - \frac{\partial U^*_R}{\partial U_R}\right), \end{aligned} \tag{75}$$

where

$$U^*_L = \frac{1}{S_M - S_L}[F_L - S_L U_L - (0, 0, p^*, S_M.P^*)^T], \tag{76}$$

$$U^*_R = \frac{1}{S_M - S_R}[F_R - S_R U_R - (0, 0, p^*, S_M.P^*)^T], \tag{77}$$

$$\frac{\partial U^*_L}{\partial U_L} = \frac{\left(\frac{\partial F_L}{\partial U_L} - S_L - \frac{\partial}{\partial U_L}(0,0,p^*,S_M.P^*)^T\right)(S_M - S_L) - (F_L - S_L U_L - (0,0,P^*,S_M.p^*)^T)\frac{\partial S_M}{\partial U_L}}{(S_M - S_L)^2}, \tag{78}$$

$$\frac{\partial U^*_L}{\partial U_R} = \frac{-\frac{\partial}{\partial U_L}((0,0,p^*,S_M.p^*)^T)(S_M - S_L) - (F_L - S_R U_L - (0,0,P^*,S_M.P^*)^T)\frac{\partial S_M}{\partial U_R}}{(S_M - S_L)^2}, \tag{79}$$

$$\frac{\partial U^*_R}{\partial U_L} = \frac{-\frac{\partial}{\partial U_L}((0,0,p^*,S_M.p^*)^T)(S_M - S_R) - (F_R - S_R U_R - (0,0,P^*,S_M.P^*)^T)\frac{\partial S_M}{\partial U_L}}{(S_M - S_R)^2}, \tag{80}$$

$$\frac{\partial U^*_R}{\partial U_R} = \frac{\left(\frac{\partial F_R}{\partial U_R} - S_R - \frac{\partial}{\partial U_R}(0,0,p^*,S_M.P^*)^T\right)(S_M - S_R) - (F_R - S_R U_R - (0,0,P^*,S_M.P^*)^T)\frac{\partial S_M}{\partial U_R}}{(S_M - S_R)^2}. \tag{81}$$

Using Relations (32) and (33), and $P^*_L = P^*_R = P^*$, two expressions for P^* are obtained:

$$P^* = F_L(2) - S_L U_L(2) - S_M(F_L(1) - S_L U_L(1)) \tag{82}$$

and

$$P^* = F_R(2) - S_R U_R(2) - S_M(F_R(1) - S_R U_R(1)). \tag{83}$$

To have a more symmetric derivative, the following average expression is used:

$$P^* = \frac{F_R(2) - S_R U_R(2) - S_M(F_R(1) - S_R U_R(1)) + F_L(2) - S_L U_L(2) - S_M(F_L(1) - S_L U_L(1))}{2}. \tag{84}$$

Its derivatives read,

$$\frac{\partial P^*}{\partial U_L} = \frac{1}{2}\left[\frac{\partial F_L(2)}{\partial U_L} - S_L(0,0,1,0)^T - S_M\left(\frac{\partial F_L(1)}{\partial U_L} - S_L(0,1,0,0)^T\right) - (F_L(1) - S_L U_L(1))\frac{\partial S_M}{\partial U_L}\right], \tag{85}$$

$$\frac{\partial P^*}{\partial U_R} = \frac{1}{2}\left[\frac{\partial F_R(2)}{\partial U_R} - S_R(0,0,1,0)^T - S_M\left(\frac{\partial F_R(1)}{\partial U_R} - S_R(0,1,0,0)^T\right) - (F_R - S_R U_R)\frac{\partial S_M}{\partial U_R}\right]. \tag{86}$$

The contact wave speed is given by,

$$S_M = \frac{S_R U_R(2) - S_L U_L(2) - (F_R(2) - F_L(2))}{S_R U_R(1) - S_L U_L(1) - (F_R(1) - F_L(1))}. \tag{87}$$

Its derivative are given by,

$$\frac{\partial S_M}{\partial U_L} = \frac{\left(\frac{\partial F_L(2)}{\partial U_L} - S_L\frac{\partial U_L(2)}{\partial U_L}\right)(S_R U_R(1) - S_L U_L(1) - (F_R(1) - F_L(1)))}{(S_R U_R(1) - S_L U_L(1) - (F_R(1) - F_L(1)))^2} - \frac{(S_R U_R(2) - S_L U_L(2) - (F_R(2) - F_L(2)))\left(\frac{\partial F_L(1)}{\partial U_L} - S_L\frac{\partial U_L(1)}{\partial U_L}\right)}{(S_R U_R(1) - S_L U_L(1) - (F_R(1) - F_L(1)))^2} \tag{88}$$

$$\frac{\partial S_M}{\partial U_R} = \frac{\left(S_R\frac{\partial U_R(2)}{\partial U_R} - \frac{\partial F_R(2)}{\partial U_R}\right)(S_R U_R(1) - S_L U_L(1) - (F_R(1) - F_L(1)))}{(S_R U_R(1) - S_L U_L(1) - (F_R(1) - F_L(1)))^2} - \frac{(S_R U_R(2) - S_L U_L(2) - (F_R(2) - F_L(2)))\left(S_R\frac{\partial U_R(1)}{\partial U_R} - \frac{\partial F_R(1)}{\partial U_R}\right)}{(S_R U_R(1) - S_L U_L(1) - (F_R(1) - F_L(1)))^2} \tag{89}$$

These various derivatives require the knowledge of $\frac{\partial F_L}{\partial U_L}$ and $\frac{\partial F_R}{\partial U_R}$. They correspond to the Jacobian matrix of the considered System which requires the derivatives of the mixture pressure.

The mixture pressure reads,

$$P = \frac{1}{2}(A_1 + A_2 - (P_{\infty,1} + P_{\infty,2})) + \sqrt{\frac{1}{4}(A_2 - A_1 - (P_{\infty,2} - P_{\infty,1}))^2 + A_1 A_2}, \tag{90}$$

where $A_k = \frac{Y_k(\gamma_k - 1)C v_k}{Y_1 C v_1 + Y_2 C v_2}(\rho(e-q) - P_{\infty,k})$.

Thus, the corresponding derivatives read,

$$\frac{\partial P}{\partial U} = \frac{1}{2}\left(\frac{\partial A_1}{\partial U} + \frac{\partial A_2}{\partial U}\right) + \frac{\frac{1}{2}\left[\frac{1}{2}\left(\frac{\partial A_2}{\partial U} - \frac{\partial A_1}{\partial U}\right)(A_2 - A_1 - (P_{\infty,2} - P_{\infty,1})) + A_1\frac{\partial A_2}{\partial U} + A_2\frac{\partial A_1}{\partial U}\right]}{\sqrt{\frac{1}{4}(A_2 - A_1 - (P_{\infty,2} - P_{\infty,1}))^2 + A_1 A_2}}, \tag{91}$$

where

$$\frac{\partial A_k}{\partial U} = (\rho(e-q) - P_{\infty,k})\left[\frac{\frac{\partial y_k}{\partial U}(\gamma_k - 1)C_{v,k}\rho(y_k(C_{v,1} - C_{v,2}) + \rho C_{v,2}) - y_k(\gamma_k - 1)C_{v,k}\left(\frac{\partial \rho}{\partial U}(y_1(C_{v,1} - C_{v,2})C_{v,2}) + \rho(C_{v,1} - C_{v,2})\frac{\partial y_1}{\partial U}\right)}{(y_1 C_{v,1} + y_2 C_{v,2})^2}\right] + \frac{y_k(\gamma_k - 1)C_{v,k}}{\rho y_1(C_{v,1} - C_{v,2}) + \rho C_{v,2}}\left(\frac{\partial \rho e}{\partial U} - \frac{\partial \rho q}{\partial U}\right), \tag{92}$$

with

$$y_k = \rho Y_k$$
$$\rho e = \rho E - \frac{(\rho u)^2}{\rho} - \frac{(\rho v)^2}{\rho},$$
$$\rho q = y_1 q_1 + y_2 q_2.$$

Appendix D. Heat flux derivatives

The derivatives appearing in the heat conduction term read:

$$\frac{\partial q_{i,i+1/2}}{\partial U_i} = \frac{\lambda_{eq,i}\lambda_{eq,i+1}}{\frac{1}{2}\Delta x(\lambda_{eq,i} + \lambda_{eq,i+1})}\frac{\partial T_i}{\partial U_i} - \frac{T_{i+1} - T_i}{\frac{1}{2}\Delta x}\frac{\partial}{\partial U_i}\left(\frac{\lambda_{eq,i}\lambda_{eq,i+1}}{\lambda_{eq,i} + \lambda_{eq,i+1}}\right), \tag{93}$$

$$\frac{\partial q_{i,i+1/2}}{\partial U_{i+1}} = -\frac{\lambda_{eq,i}\lambda_{eq,i+1}}{\frac{1}{2}\Delta x(\lambda_{eq,i} + \lambda_{eq,i+1})}\frac{\partial T_{i+1}}{\partial U_{i+1}} - \frac{T_{i+1} - T_i}{\frac{1}{2}\Delta x}\frac{\partial}{\partial U_{i+1}}\left(\frac{\lambda_{eq,i}\lambda_{eq,i+1}}{\lambda_{eq,i} + \lambda_{eq,i+1}}\right), \tag{94}$$

$$\frac{\partial q_{i,i-1/2}}{\partial U_i} = -\frac{\lambda_{eq,i-1}\lambda_{eq,i}}{\frac{1}{2}\Delta x(\lambda_{eq,i-1} + \lambda_{eq,i})}\frac{\partial T_i}{\partial U_i} - \frac{T_i - T_{i-1}}{\frac{1}{2}\Delta x}\frac{\partial}{\partial U_i}\left(\frac{\lambda_{eq,i-1}\lambda_{eq,i}}{\lambda_{eq,i-1} + \lambda_{eq,i}}\right), \tag{95}$$

$$\frac{\partial q_{i,i-1/2}}{\partial U_{i-1}} = \frac{\lambda_{eq,i-1}\lambda_{eq,i}}{\frac{1}{2}\Delta x(\lambda_{eq,i-1} + \lambda_{eq,i})}\frac{\partial T_{i-1}}{\partial U_{i-1}} - \frac{T_i - T_{i-1}}{\frac{1}{2}\Delta x}\frac{\partial}{\partial U_{i-1}}\left(\frac{\lambda_{eq,i-1}\lambda_{eq,i}}{\lambda_{eq,i-1} + \lambda_{eq,i}}\right), \tag{96}$$

with

$$\frac{1}{T} = \frac{\rho Y_1(\gamma_1 - 1)C_{v,1}}{P + P_{\infty,1}} + \frac{\rho Y_2(\gamma_2 - 1)C_{v,2}}{P + P_{\infty,2}}, \tag{97}$$

$$\frac{\partial \lambda_{eq,i}}{\partial U_i} = \lambda_1\frac{\partial \alpha_{i,1}}{\partial U_i} + \lambda_2\frac{\partial \alpha_{i,2}}{\partial U_i}, \tag{98}$$

$$\frac{\partial T_i}{\partial U_i} = -T_i^2\left[(\gamma_1 - 1)C_{v,1}\left(\frac{\frac{\partial y_{i,1}}{\partial U_i}(P_i + P_{\infty,1}) - y_{i,1}\frac{\partial P_i}{\partial U_i}}{(P_i + P_{\infty,1})^2} + \right)\right] + T_i^2\left[(\gamma_2 - 1)C_{v,2}\left(\frac{\frac{\partial y_{i,2}}{\partial U_i}(P_i + P_{\infty,2}) - y_{i,2}\frac{\partial P_i}{\partial U_i}}{(P_i + P_{\infty,2})^2} + \right)\right], \tag{99}$$

where

$$y_{i,k} = \rho Y_k, \tag{100}$$

$$\frac{\partial \alpha_{i,k}}{\partial U_i} = \frac{\partial \frac{y_{i,k}}{\rho_k}}{\partial U_i},$$
$$\frac{\partial \alpha_{i,k}}{\partial U_i} = (\gamma_k - 1)C_{v,k}\left[\frac{\left(T_i\frac{\partial y_{i,k}}{\partial U_i} + y_{i,k}\frac{\partial T_i}{\partial U_i}\right)(P_i + P_{\infty,k}) - y_{i,k}T_i\frac{\partial P_i}{\partial U_i}}{(P_i + P_{\infty,k})^2}\right]. \tag{101}$$

The pressure derivative, $\frac{\partial P_i}{\partial U_i}$, is computed using Relation (91)

Appendix E. Surface and body forces derivatives

- The derivatives corresponding to the surface tension effects are first considered:

The curvature, κ_{ij}^n, being taken constant in each cell, expression (45) is used to obtain the derivatives:

$$\frac{\partial \overrightarrow{\nabla C}_{ij}^n}{\partial U_{ij}} = 0, \quad \frac{\partial \overrightarrow{\nabla C}_{ij}^n}{\partial U_{i-1j}} = -\frac{1}{2\Delta x}\frac{\partial C_{i-1j}^n}{\partial U_{i-1j}}, \quad \frac{\partial \overrightarrow{\nabla C}_{ij}^n}{\partial U_{i+1j}} = \frac{1}{2\Delta x}\frac{\partial C_{i+1j}^n}{\partial U_{i+1j}}, \tag{102}$$

$$\frac{\partial \overrightarrow{\nabla C}_{ij}^n}{\partial U_{ij-1}} = -\frac{1}{2\Delta y}\frac{\partial C_{ij-1}^n}{\partial U_{ij-1}}, \quad \frac{\partial \overrightarrow{\nabla C}_{ij}^n}{\partial U_{ij+1}} = \frac{1}{2\Delta y}\frac{\partial C_{ij+1}^n}{\partial U_{ij+1}}. \tag{103}$$

The colour function being part of the unknown vector U, its derivative is very simple.

- The derivatives corresponding to the gravity term read:

$$\frac{\partial \rho_{ij}\mathbf{g}}{\partial U_{ij}} = \mathbf{g}\frac{\partial \rho_{ij}}{\partial U_{ij}}, \tag{104}$$

$$\frac{\partial \rho_{ij}\mathbf{g}\bullet\mathbf{u}_{ij}}{\partial U_{ij}} = \mathbf{g}\frac{\partial \rho_{ij}\mathbf{u}}{\partial U_{ij}}. \tag{105}$$

Variables ρ_{ij} and $\rho_{ij}\mathbf{u}$ being part of the unknown vector U, their derivatives are straightforward.

References

Allaire, G., Faccanoni, G., Kokh, S., 2007. A strictly hyperbolic equilibrium phase transition model. Comptes Rendus Mathematique 344, 135–140.

Anderson, D., McFadden, G., Wheeler, A., 1998. Diffuse-interface methods in fluid mechanics. Ann. Rev. Fluid Mech. 30, 139–165.

Balay, S., Gropp, W.D., McInnes, L.C., Smith, B.F., 1997. Efficient management of parallelism in object oriented numerical software libraries. In: Arge, E., Bruaset, A.M., Langtangen, H.P. (Eds.), Modern Software Tools in Scientific Computing. Birkhäuser Press, pp. 163–202.

Balay, S., Brown, J., Buschelman, K., Eijkhout, V., Gropp, W.D., Kaushik, D., Knepley, M.G., McInnes, L.C., Smith, B.F., Zhang, H., 2013a. PETSc Users Manual. Technical Report ANL-95/11 - Revision 3.4. Argonne National Laboratory.

Balay, S., Brown, J., Buschelman, K., Gropp, W.D., Kaushik, D., Knepley, M.G., McInnes, L.C., Smith, B.F., Zhang, H., 2013b. PETSc Web page. <http://www.mcs.anl.gov/petsc>.

Brackbill, J., Kothe, D., Zemach, C., 1992. A continuum method for modeling surface tension. J. Comput. Phys. 100, 335–354.

Braconnier, B., Nkonga, B., 2009. An all-speed relaxation scheme for interface flows with surface tension. J. Comput. Phys. 228, 5722–5739.

Cahn, J., Hilliard, J., 1958. Free energy of a nonuniform system. Part I: Interfacial free energy. J. Chem. Phys. 28, 258.

Clavin, P., Garcia, P., 1983. The influence of the temperature dependence of diffusivities on the dynamics of flame fronts. Journal de Mécanique Théorique et Appliquée 2, 245–263.

Davis, S., 1988. Simplified second-order Godunov-type methods. SIAM J. Sci. Stat. Comput. 9, 445–473.

Favrie, N., Gavrilyuk, S., Saurel, R., 2009. Solid–fluid diffuse interface model in cases of extreme deformations. J. Comput. Phys. 228, 6037–6077.

Guillard, H., Viozat, C., 1999. On the behaviour of upwind schemes in the low Mach number limit. Comput. Fluids 28, 63–86.

Harten, A., Lax, P., van Leer, B., 1983. On upstream differencing and Godunov-type schemes for hyperbolic conservation laws. SIAM Rev. 25, 35–61.

Jamet, D., Lebaigue, O., Coutris, N., Delhaye, J.M., 2001. The second gradient method for the direct numerical simulation of liquid–vapor flows with phase change. J. Comput. Phys. 169, 624–651.

Juric, D., Tryggvason, G., 1998. Computations of boiling flows. Int. J. Multiphase Flow 24, 387–410.

Kapila, A., Menikoff, R., Bdzil, J., Son, S., Stewart, D., 2001. Two-phase modeling of deflagration-to-detonation transition in granular materials: Reduced equations. Phys. Fluids 13, 3002–3024.

LeMartelot, S., Nkonga, B., Saurel, R., 2013. Liquid and liquid–gas flows at all speed. J. Comput. Phys. 255, 53–82.

Le Métayer, O., Massoni, J., Saurel, R., 2004. Élaboration des lois d'état d'un liquide et de sa vapeur pour les modèles d'écoulements diphasiques. Int. J. Thermal Sci. 43, 265–276 (in French).

Perigaud, G., Saurel, R., 2005. A compressible flow model with capillary effects. J. Comput. Phys. 209, 139–178.

Petitpas, F., Massoni, J., Saurel, R., Lapebie, E., Munier, L., 2009. Diffuse interface model for high speed cavitating underwater systems. Int. J. Multiphase Flow 35, 747–759.

Petitpas, F., Saurel, R., Franquet, E., Chinnayya, A., 2009. Modelling detonation waves in condensed energetic materials: multiphase CJ conditions and multidimensionnal computations. Shock Waves 19, 377–401.

Saad, Y., 1992. Numerical Methods for Large Eigenvalue Problems. Manchester University Press.

Saurel, R., Abgrall, R., 1999. A multiphase Godunov method for multifluid and multiphase flows. J. Comput. Phys. 150, 425–467.

Saurel, R., Le Métayer, O., Massoni, J., Gavrilyuk, S., 2007. Shock jump relations for multiphase mixtures with stiff mechanical relaxation. Shock Waves 16, 209–232.

Saurel, R., Petitpas, F., Abgrall, R., 2008. Modelling phase transition in metastable liquids: application to cavitating and flashing flows. J. Fluid Mech. 607, 313–350.

Saurel, R., Petitpas, F., Berry, R., 2009. Simple and efficient methods relaxation for interfaces separating compressible fluids, cavitating flows and shocks in multiphase mixtures. J. Comput. Phys. 228, 1678–1712.

Schoch, S., Nikiforakis, N., Lee, B.J., Saurel, R., 2013. Multi-phase simulation of ammonium nitrate emulsion detonations. Combust. Flame 160, 1883–1899.

Shukla, R., Pantano, C., Freund, J., 2010. An interface capturing method for the simulation of multi-phase compressible flows. J. Comput. Phys. 229, 7411–7439.

Toro, E., Spruce, M., Speares, W., 1994. Restoration of the contact surface in the HLL-Riemann solver. Shock Waves 4, 25–34.

Tryggvason, G., Bunner, B., Esmaeeli, A., Juric, D., Al-Rawahi, N., Tauber, W., Han, J., Nas, S., Jan, Y.-J., 2001. A front-tracking method for the computations of multiphase flow. J. Comput. Phys. 169, 708–759.

Turkel, E., 1987. Preconditioned methods for solving the incompressible and low speed compressible equations. J. Comput. Phys. 72, 277–298.

Wood, A.B., 1930. A textbook of Sound. Bell Eds.